PNAS
www.pnas.org

Supplementary Information for

Subglacial meltwater supported oxygenated marine habitats during Snowball Earth

Maxwell Lechte, Malcolm Wallace, Ashleigh van Smeerdijk Hood, Weiqiang Li, Ganqing Jiang, Galen Halverson, Dan Asael, Stephanie McColl & Noah Planavsky
Email: maxwell.lechte@mail.mcgill.ca

This PDF file includes:

Other Supplementary Materials for this manuscript include the following:

Dataset S1 [Electron microprobe data; LA-ICP-MS data; XRF data; ICP-MS data; Fe isotope data; results of statistical analyses]

www.pnas.org/cgi/doi/10.1073/pnas.1909165116

Supplementary Materials and Methods

Petrography and microscopy

Field work on Cryogenian iron formations and associated glacial successions was conducted in nine study areas on three continents. Multiple stratigraphic sections were measured at each locality for facies analysis and sample collection. Iron formation samples were collected from surface outcrop from the Chuos Formation in central and northern Namibia (n = 22), the Yudnamutana Subgroup of South Australia (n = 52) and the Kingston Peak Formation in the Death Valley and Kingston Range regions of California (n = 59) for petrographic and geochemical analysis. Samples with joints, veins or excess weathering were avoided in order to best target the primary, least-altered chemical sediment.

In situ elemental analyses

All samples were prepared as polished thick (~100 μm) thin sections and petrographically analyzed using reflected light microscopy as well as scanning electron microscopy (SEM) carried out on a Philips FEI XL30 environmental SEM at the School of Earth Sciences (University of Melbourne). Following petrographic analysis, samples were selected for spatially resolved *in situ* geochemical analyses (Chuos Formation n = 18; Yudnamutana Subgroup n = 48; Kingston Peak Formation n = 27). The most pristine spots were selected for *in situ* analysis using reflected light microscopy, with multiple spots selected for each sample (Chuos Formation n = 56; Yudnamutana Subgroup n = 184; Kingston Peak Formation n = 92).

Electron microprobe analyses were performed at the School of Earth Sciences (University of Melbourne) using a Cameca SX50 Electron Microprobe, with an accelerating voltage of 15 kV, beam current of 35 nA, spot size of 25 μm and a count time of 80 s. Limits of detection were generally better than 0.05 elemental wt. % for all elements analyzed. Reference materials MGOX, ALOX, WOL9 and HEM6 were used as calibration standards.

The same spots analyzed by the electron microprobe were analyzed for trace element contents using laser ablation-inductively coupled plasma-mass spectrometry (LA-ICP-MS). Analyses were carried out on a Helex 193 nm ArF excimer laser ablation system connected to an Agilent 7700X quadrupole ICP-MS as the School of Earth Sciences (University of Melbourne). Operating conditions included a source sample rate of 1.7 Hz, an ablation time of 60 s and a 72 μm spot size. United States Geological Survey international standards BCR-2 and BHVO-2, and National Institute of Standards standard reference material NIST612, were analyzed regularly throughout the sequence. LA-ICP-MS data was reduced using Iolite Software (1) following the Trace Elements Scheme (2). Silicon and iron elemental values, determined via electron microprobe analysis, were used as an internal standard depending on which was in greater abundance for each spot analysis. For REEY analysis, data was normalized to upper continental crust (UCC) using values from Queensland Mud (MuQ; Kamber et al. 3).

Bulk rock elemental analyses

All samples (n = 133) were cut to remove all weathered surfaces, and all cut faces were subsequently cleaned with carborundum paper to avoid contamination from the rock saw. Cut samples were crushed to gravel size using a rock hammer, using a thick paper towel to avoid direct contact between metal surfaces and the samples, and crushed to a fine (<5 μm) powder using an agate ring mill.

For bulk rock elemental analysis, powders from the Chuos Formation (n = 22), Yudnamutana Subgroup (n = 8) and the Kingston Peak Formation (n = 59) samples were prepared as fused glass discs using a mixed lithium metaborate/tetraborate flux and analyzed using a SPECTRO Xepos Energy Dispersive X-ray fluorescence (XRF) spectrometer at the School of Earth Sciences (University of Melbourne). A range of internationally certified reference materials were used for analytical calibration. Powders from Yudnamutana Subgroup (n = 52) and Kingston Peak Formation (n = 59) samples were weighed and digested in a two-step (concentrated HF-HNO_3 and HNO_3-HCl) method for total digest. Splits from each sample solution were analyzed for major and trace element concentrations using a ThermoFinnegan Scientific Element XR inductively coupled plasma-mass spectrometer (ICP-MS) at the

Yale Metal Geochemistry Center. Elemental precision was better than 5% for duplicate geostandards (BHVO).

Bulk rock Fe isotope analyses

Iron isotope compositions are reported using conventional delta notation relative to the IRMM-14 standard:

$$\delta^{56}\mathrm{Fe}(‰) = \left[\frac{(^{56}\mathrm{Fe}/^{54}\mathrm{Fe})_{sample}}{(^{56}\mathrm{Fe}/^{54}\mathrm{Fe})_{IRMM-14}} - 1\right] \times 1000$$

Samples from the Yudnamutana Subgroup (n = 33) and the Kingston Peak Formation (n = 29) were selected for Fe isotope analysis and purified using ion-exchange chromatography with AG MP-1 M resin (methods modified from 4). For mass spectrometry, we followed the methods of Busigny et al. (5), with minor modifications. We used a CETAC AridusII desolvating nebulizer and introduced a 1 ppm purified Fe solution. Iron isotope measurements were made on a ThermoFisher Scientific Neptune Plus Multi-Collector ICP-MS at the Yale Metal Geochemistry Center. The analytical blank was always below 35 ng Fe and represented an insignificant portion of the processed Fe. Therefore, no blank corrections were made. Fe isotope results were bracketed by, and reported relative to, the IRMM-14 standard. Average sample standard error (2SE) was 0.027 ‰ (*SI Appendix*, Data S1). Full protocol error, based on duplicate samples and processed IRMM-14 standards, was better than 0.1 ‰. The geostandards BHVO-2 (0.11 ‰ ± 0.15 2 standard deviation; 2SD, n = 6) and NOD-A-1 (-0.41 ‰ ± 0.14 2SD, n = 3) were measured throughout the run and are comparable to published values for BHVO-2 (0.13 ‰ ± 0.02 2SD; 6) and NOD-A-1 (-0.42 ‰ ± 0.07 2SD; 7). Sample yields were generally greater than 97 %.

Samples from the Chuos Formation (n = 37), Yudnamutana Subgroup (n = 7) and Kingston Peak Formation (n = 1) were selected for Fe isotope analysis conducted at the State Key Laboratory for Mineral Deposit Research (Nanjing University). Iron isotope ratios were measured using a Thermo Fisher Scientific Neptune Plus Multi-Collector ICP-MS at the State Key Laboratory for Mineral Deposit Research (Nanjing University); details of the analytical procedures can be found in Du et al. (8) and Ye et al. (9). Iron was purified using ion exchange chromatography and the recovery of Fe was greater than 95 %. The typical internal precision (2SE) was better than ± 0.03 ‰ for $^{56}Fe/^{54}Fe$. The long-term external reproducibility (2SD) of Fe isotope analysis is better than ± 0.06 ‰ for $^{56}Fe/^{54}Fe$ and ± 0.16‰ for $^{57}Fe/^{54}Fe$, based on repeat analysis of multiple Fe isotope standard solutions against in-house stock solutions. The measured $\delta^{56}Fe$ values of two ultrapure Fe solutions from University of Wisconsin-Madison, J-M Fe and HPS Fe, are 0.31 ± 0.03 ‰ (n = 6, 2SD) and 0.59 ± 0.02 ‰ (n = 6, 2SD), respectively, which are in excellent agreement with the recommended values (10). In addition, the measured Fe isotope compositions of the international whole-rock standards BHVO-2 ($\delta^{56}Fe$ = 0.09 ± 0.01 ‰, n = 3), BCR-2 ($\delta^{56}Fe$ = 0.06 ± 0.01 ‰, n = 3), DNC-1a ($\delta^{56}Fe$ = 0.04 ± 0.02 ‰, n = 3), DTS-2b ($\delta^{56}Fe$ = 0.03 ± 0.04 ‰, n = 3) and BIR-1a ($\delta^{56}Fe$ = 0.11 ± 0.04 ‰, n = 3), are all consistent with the recommended values (11) within analytical uncertainties.

Supplementary Information Text

Geological setting

The study localities of Cryogenian IF-bearing glacial successions were chosen based upon a number of factors, including exceptional preservation of Cryogenian glacial successions, clear sedimentological and stratigraphic constraints on the depositional setting, and the presence of IFs and other ferruginous lithologies throughout the sedimentary package. Nine localities were selected as case studies on three separate Cryogenian formations: four study areas on the Chuos Formation of northern Namibia, three study areas of the Yudnamutana Subgroup, South Australia, and two study areas of the Kingston Peak Formation, California.

Chuos Formation

The Chuos Formation (12) outcrops throughout central and northern Namibia (Fig. S1A) and comprises a glacially influenced sedimentary succession correlated to the Sturtian glaciation (13, 14), which is considered to have occurred 717–660 Ma (15, 16). The underlying volcanics of the Naauwpoort Formation have yielded a zircon U-Pb isotope dilution-thermal ionization mass spectrometry (ID-TIMS) age of 746 ± 2 Ma (17). The Chuos Formation accumulated in a series of marine rift basins during the rifting of Rodinia (18), and locally exceeds 2000 m in thickness (14). One locality in northern Namibia was studied near the village Okavare (Fig. S1B). Three localities in central Namibia were also studied: Mitten Fold near the village Orusewa, south of the Fransfontein Ridge, and at the Rondehoek Fold on the farm Lowenfontein (Fig. S1C-E).

In central Namibia, the Chuos Formation is part of the Swakop Group. Here the Chuos Formation is bounded at each study locality by unconformities that likely represent a significant time gap, and overlain by Ediacaran carbonates. In northern Namibia, the Chuos Formation is part of the correlative Otavi Group and in the study area unconformably overlies the Ombombo Subgroup and is overlain by the postglacial carbonates of the Rasthof Formation, considered to be the Sturtian cap carbonate (19). The Neoproterozoic strata of Namibia were deformed during the ca. 580 Ma Damaran Orogeny which formed a series of Pan-African orogenic belts (20). These orogenic belts include the Damara Belt of central Namibia, the Kaoko Belt to the northwest and the Gariep Belt of southern Namibia (18). The Northern Margin Zone of the Damara Belt and the Northern Platform of the Kaoko Belt are collectively referred to as the Otavi Fold Belt (21).

In the study areas the Chuos Formation has experienced low-mid greenschist facies metamorphism, with magnetite replacing hematite in some of the IFs (22). As a result, the dominant Fe-bearing phase in the Chuos IF is porphyroblastic magnetite which can be seen to be locally replacing microcrystalline hematite (22). The similarity of the geochemical profile of the magnetite versus the hematite in the Chuos IFs suggests that this transformation is mostly isochemical, as documented in an *in situ* trace element study of other Neoproterozoic IFs (23). Chert is also abundant in the Chuos IFs, with minor siderite, apatite, dolomite and detrital quartz grains also present. Bedded chert and jaspilite are also present in the Chuos IF. A detailed lithological description can be found in Lechte et al. (22).

Yudnamutana Subgroup

The Yudnamutana Subgroup is the Sturtian glacial succession (24) of the Adelaide Fold Belt of South Australia (Fig. S4A), of which the IF-bearing middle formation is referred to as the Holowilena Ironstone (25). A U-Pb zircon chemical abrasion ID-TIMS age of 663 ± 0.1 Ma from a tuff horizon in the uppermost Yudnamutana Subgroup constraints the timing of the end of glacial deposition (26). The Yudnamutana Subgroup is interpreted to have been deposited in the marine rift complex of the Barratta Trough during the break-up of the Rodinia supercontinent (27). Three localities were chosen for in-depth stratigraphic and sedimentological analysis: Oraparinna in the Ikara-Flinders Ranges, Willippa (east of Hawker), and Holowilena South (east of Craddock; Fig. S4B-D).

The basal formation of the Yudnamutana Subgroup in the study areas is the Pualco Tillite, which unconformably overlies the Burra Group and is considered to represent the onset of glaciation (28). Locally,

the Pualco Tillite is overlain by the Holowilena Ironstone which is often lenticular and regionally discontinuous on the kilometer scale (29). The Holowilena Ironstone is overlain by the Wilyerpa Formation, a thick (<2000 m) glaciogenic succession of siltstone, dolomite and diamictite with abundant ice-rafted debris (29, 30) that comprises the terminal Yudnamutana Subgroup. The Yudnamutana Subgroup is overlain by the Tindelpina Shale Member of the Tapley Hill Formation, considered to be the Sturtian cap carbonate equivalent (31) recording the onset of postglacial sedimentation (32). In the Oraparinna area, the Yudnamutana Subgroup is in faulted contact with a dolomitic breccia, likely brecciated carbonates of Callanna Beds uplifted by diapiric activity. The Neoproterozoic–Cambrian strata of South Australia were deformed to form the Adelaide Fold Belt during the Cambrian–Ordovician Delamerian Orogeny (33).

The Yudnamutana IFs are predominantly composed of fine-grained (~5 μm) hematite and microcrystalline quartz, with minor clay minerals, quartz and feldspar grains. The majority of these IFs are finely laminated ferhythmite (sensu Beukes and Gutzmer; 34), although mesobanded jaspilite is also present (29). Although the correlative Braemar Ironstone of the central Flinders Ranges features a metamorphic overprint of porphyroblastic magnetite (35), the Holowilena Ironstone is well preserved and has experienced negligible to sub-greenschist facies metamorphism in the study areas. A full description of the mineralogy, sedimentology and stratigraphy of the Holowilena Ironstone can be found in Lechte and Wallace (29).

Kingston Peak Formation

The Kingston Peak Formation (36) represents the entire Cryogenian stratigraphy of the Death Valley region, California (Fig. S7A). The Kingston Peak Formation is the uppermost formation of the Stenian–Cryogenian Pahrump Group, and overlies the Tonian Beck Spring Dolomite. Two study areas were selected in southeast Death Valley and the southern Kingston Range Wilderness based upon the abundance and preservation of IFs at these localities.

The Kingston Peak Formation in the Death Valley region is subdivided into four members: the lower (KP1), middle (KP2), upper (KP3) and a localized top (KP4) member. The lowermost member of the Kingston Peak Formation (KP1) comprises limestones and siltstones that lack evidence of glacial activity and are considered pre-glacial and related to the underlying Beck Spring Dolomite (37). Members KP2 and KP3 are glaciogenic and typically correlated with the Sturtian glacial succession, although this correlation lacks robust geochronological constraints (37). There is debate regarding whether the localized top member (KP4) represents deposition during the Marinoan glaciation (37, 38), however, this member is not present in the study areas. The Noonday Formation overlies the Kingston Peak Formation in variously conformable and unconformable contact, and is considered to represent the Marinoan cap carbonate (38). The Death Valley region experienced deformation during the Mesozoic Cordilleran orogeny (39) and extension during the Neogene (40) that led to the regional emplacement of felsic intrusions and the establishment of the modern basin and range setting.

The mineralogy of the Kingston Peak IFs is simple, consisting predominantly of hematite with minor clays, chert, chlorite and magnetite (41). The Kingston Peak Formation in the study areas is well preserved and has experienced negligible to sub-greenschist facies metamorphism (41). A comprehensive description of the sedimentology and stratigraphy of the Kingston Peak IFs can be found in Lechte et al. (41).

Glacial systems

Glacial sedimentology

The interbedded glacial and marine strata in the studied Cryogenian successions are indicative of deposition in a glaciomarine environment, and comparisons to modern glaciomarine sediments is important for interpreting the paleoenvironment of these deposits. Facies variability in proglacial marine environments is largely controlled by the distance from the ice margin or grounding line (42-47). Although classification schemes vary, glaciomarine sediments can be categorized into facies that correspond to three broad depositional settings: ice-contact, ice-proximal and ice-distal (48).

Ice-contact facies sediments are deposited in terminoglacial settings (49) up to a few kilometers from the grounding line (49-51). This facies predominantly features massive to crudely stratified, coarse-grained diamictites deposited as subglacial diamict, melt-out diamict and tunnel-mouth outwash deposits close to meltstream exits (43, 45, 49, 52). Subglacial diamict is typically massive and clast-rich, featuring a wide range of clast sizes up to boulder size (47, 52, 53). Subglacial deformation can lead to the deposition of lodgement and deformation till. Glaciotectonic deformation features include soft sediment shear structures, rotational structures and an upwards-gradational increase in deformation due to basal shear (52, 54), with erosional unconformities common (43). Melt-out diamictites are poorly sorted and lack internal structure, often with sharp conformable contacts (42, 52, 55), and build up as morainal banks or grounding zone wedges (51, 56). Submarine glaciofluvial processes can also deposit gravelly sand, often with subrounded clasts, which can build up as grounding-line fans. Due to the high erosive power of grounded ice sheets, preservation potential is low in ice-contact settings (42).

The ice-proximal facies is deposited in the proglacial marine environment (49), up to ~10 km from the grounding line. This represents a transitional facies between the ice-contact and ice-distal environments, and can feature sediments common to both settings (49). Characteristic lithologies include ice-rafted debris, meltwater suspension settling and mass flow resedimented deposits such as glaciogenic debris flows and glacioturbidites (46, 57). Proglacial fans can develop as a result of stacked outwash and debris flow deposits, and slump facies and other soft sediment deformation features are common under high accumulation rates. Graded diamictites and sandstones are more common than massive diamictites, as opposed to the terminoglacial environment. Subglacial deformation and lodgement till are not deposited in the proglacial environment.

The ice-distal facies is deposited in the extraglacial marine environment (49), i.e. beyond the proglacial environment, and glacially influenced sediments may be deposited up to thousands of kilometers from the grounding line due to ice rafting (43, 51). In the extraglacial environment marine sedimentary processes dominate (42), and full-marine facies sediments are often interbedded with siltstones and sandstones deposited due to the settling of suspended sediment plumes and turbidity currents (43, 50). Coarse-grained material can be supplied via glacially influenced submarine fans (58). Glaciogenic debris flows can also be deposited in this setting; these tend to form blanket-like, graded diamictites or conglomerates that thicken in bathymetric depressions (43).

Outsized clasts or lonestones that deflect and/or pierce underlying laminae, and feature onlapping overlying laminae, are interpreted as dropstones and therefore unequivocal evidence of a glacial influence on deposition. Iceberg rafting in modern polar environments can extend for thousands of kilometers from the ice margin, and ice-rafted debris can theoretically be deposited throughout all glaciomarine environments. However, the controls on distribution of ice-rafted debris within glaciomarine environments are complex (59), and the volume of debris entrained in ice shelves and icebergs can be variable. Iceberg jams in fjords can lead to the melting and deposition of icebergs in a more ice-proximal marine environment (43). Ice-rafted debris deposition in the ice-contact or ice-proximal environment is more difficult to identify as massive diamictites are more common in these settings, and lonestones within a massive matrix often cannot easily be conclusively interpreted as the product of ice-rafting.

Glaciers in modern polar environments can produce enormous volumes of meltwater (60, 61); this meltwater flux plays a key role in the sedimentological and oceanographic processes occurring in periglacial environments (62). Subglacial meltwater is expelled into the proglacial environmental at the grounding line as efflux jets, depositing coarse underflows and finer sediments via the rain-out of sediment plumes (42). In glaciomarine settings the grain size of these jet efflux deposits generally becomes finer with distance from the grounding line (42), and can involve the winnowing of fines from more proximal settings. Climate-forced variability in meltwater supply can lead to alternating sedimentary laminations defined by grainsize variations known as rhythmites (63).

Glacial hydrology and thermal regime

The hydrology and thermal regime of a glacier can control the redox state of subglacial meltwaters. The concentration of dissolved oxygen in glacial meltwaters is a function of the oxygen contents of the

atmosphere, snow and ice, dissolution rates, and the availability of reductants (64-66). The effective drainage of oxygenated subglacial meltwaters leads to elevated dissolved oxygen concentrations in glaciomarine environments (67). However, prolonged water-rock interactions, such as the biotic and abiotic oxidation of organic carbon and sulfides beneath the ice sheet, can deplete the dissolved O_2 in subglacial meltwaters (68, 69). In situations where meltwater drainage is distributed and inefficient and the underlying freshly ground substrate has an abundance of reductants (e.g. sulfides and organic matter), this can lead to anoxic subglacial (70) and proglacial (71) settings.

Glacial meltwater can be produced on the ice sheet surface, at the base of the ice sheet (due to geothermal flux and pressure), or at the base of floating ice shelves. The drainage of this meltwater can be surficial (supraglacial), internal (englacial) and basal (subglacial) (72). In some settings, supraglacial meltwater can drain to the ice sheet base via crevasses and moulin networks (73), though this process is limited in thick continental ice sheets (e.g. the Antarctic Ice Sheet) where subglacial meltwater is supplied primarily from basal melting. In addition to subglacial basal melting, ice shelf basal melting is an important source of meltwater to glaciated margins (74, 75). The highest rates of basal melting are near the grounding line, where the ice is typically above the pressure freezing point at depth (76). The supply of subglacial meltwater entrains warmer seawater and leads to higher rates of sub-ice shelf basal melt (77). The drainage of subglacial meltwater to the proglacial setting can occur via a distributed hydraulic system of basal cavities, or through a channelized system (78). Distributed systems are established when meltwater supply is low, and channelized systems are established when high meltwater flux incises into the ice and/or substrate (79, 80). Channelized meltwater systems efficiently flow to the glaciomarine environment, discharging at the grounding line as focused meltstream exits (81). Distributed systems drain far less efficiently than channelized systems, leading to longer meltwater residence times (82) and possible subglacial anoxia.

Controlled by air temperature, geothermal flux and pressure (ice thickness), glacier thermal regimes can be described as temperate (warm or wet based), cold based or polythermal (83). Wet-based glaciers have liquid water at their base, facilitating faster ice flow (84) and greater rates of erosion and sedimentation. By contrast, cold-based glaciers are frozen directly to the underlying bedrock, flowing primarily due to internal ice deformation and producing little basal meltwater. Antarctic continental shelves feature polythermal glaciers, as the base of the thick ice sheet tends to remain above the pressure melting point despite the extremely cold climate (85), whereas thinner snouts are cold based. Glaciomarine environments in Arctic fjords can be dominantly influenced by the activity of either temperature tidewater glaciers (e.g. Alaska) or polythermal glaciers (e.g. Svalbard; ref. 47).

The thermal regime of a glacial system governs the hydrology and meltwater flux and is therefore a strong control on the sedimentary processes of glaciomarine environments (47, 86). Massive diamict and subaqueous debris flow deposits are present in glaciomarine environments influenced by all types of glacial thermal regimes but are most dominant in those associated with polythermal fjord glaciers. Temperate tidewater glaciers feature abundant gravelly sand deposits as they are dominated by glaciofluvial and meltwater outwash processes (57). By contrast, meltwater outwash deposits such as grounding-line fans are less abundant in polythermal continental shelf glaciers (87). In these settings massive to stratified diamictites are deposited due to basal melt close to the grounding line, and gravel- and sand-rich facies are deposited due to sub-ice shelf rain out (87, 88). These facies can be variably associated with mass flow sediments (deposited from bottom currents and gravity flows) and laminated marine sediments (87). Although ice-rafted debris can be deposited from the basal melting of floating ice shelves (88), these deposits are generally less abundant than those deposited from debris-laden icebergs (87-89). Expansive ice shelves can feature a “null zone” of low sedimentation rates beneath the ice shelf, distal from the grounding line and iceberg calving line where ice-rafted debris is abundant (88). Biogenic sedimentation dominates modern ice-distal environments due to low clastic sedimentation rates, and diatomaceous ooze is an important constituent of Antarctic glaciated margin sediments (90). Glacial sedimentology, and the relative abundance of different glacial facies, can therefore be used to interpret the thermal regime of ancient glaciers (47).

Cryogenian iron formation depositional environment

The interpreted glacial influence on diamictite-bearing Cryogenian successions is the subject of ongoing debate (45, 91), with some researchers arguing that mass flow processes can explain Cryogenian diamictites without invoking glacial activity (92, 93). However, several studies have presented convincing sedimentological evidence for a glacial influence on deposition—including dropstones and striated clasts—for the Chuos Formation (21, 22, 54, 94), Yudnamutana Subgroup (24, 29, 30, 95, 96) and Kingston Peak Formation (38, 41, 91, 97-99). These glacial indicators, in combination with unequivocal marine sedimentary rocks, have led to a general consensus that all three of these Cryogenian successions were deposited in a glaciomarine environment (24, 30, 97, 98, 100). We further classify the IF-bearing intervals of these Cryogenian successions into distinct glaciomarine sub-environments following extensive field-based sedimentological studies of the Cryogenian stratigraphy of Namibia (22), South Australia (29) and California (41). The facies associations of these Cryogenian IFs varies stratigraphically and between outcrop belts, and each IF horizon that was sampled for analysis was classified as one of the three depositional settings (ice-contact, ice-proximal and ice-distal) described above.

At Okavare, Namibia (Fig. S2), the Chuos Formation stratigraphy is a thick succession of siltstones with rare ice-rafted debris, with discrete packages of IF and ferruginous diamictite. Rare, channelized conglomerates are interpreted as tunnel outwash deposits (101). The majority of the strata at Okavare are interpreted to have been deposited in an ice-distal to ice-proximal environment. By contrast, at Landeck (Fig. S2B), Rondehoek Fold (Fig. S2C) and Mitten Fold (Fig. S2D), ferruginous diamictites are the dominant lithology. These clast-poor to clast-rich sandy diamictites are matrix-supported with subrounded clasts and are typically massive and structureless, interpreted to have been deposited as a result of ice melt-out and subglacial outwash. Rotational structures, and elongate and fractured clasts, observed within diamictites are interpreted as subglacial deformation structures (22, 54). As such, much of the Chuos Formation strata in these areas are assigned to ice-contact to ice-proximal facies (Fig. S3).

At Holowilena South, Australia, (Fig. S4D), the Yudnamutana Subgroup stratigraphy features thick (<50 m) packages of finely laminated IF interbedded with thin (<0.5 m) jaspilite beds, turbiditic sandstone and siltstone with unidirectional ripples. A horizon of massive, ferruginous diamictites reaches up to 20 m in thickness, and graded diamictites are interpreted as muddy debris flows (29). Thus, the Holowilena Ironstone at Holowilena South is interpreted to have been deposited in an ice-proximal (rather than ice-contact) setting based upon the lower abundance of massive diamictites relative to resedimented deposits. At Oraparinna (Fig. S5), the basal Holowilena Ironstone comprises ferruginous siltstone and minor massive diamictite, interpreted to be the product of an ice-proximal setting. This diamictite-bearing package transitions into laminated ferruginous and dolomitic siltstones that feature dropstones yet lack diamictites, and these strata are interpreted to be ice-distal deposits. At Willippa (Fig. S6) the Holowilena Ironstone consists predominantly of laminated IF, jaspilite and turbiditic sandstone lacking diamictite horizons and is interpreted to be deposited in an ice-distal setting.

At Sperry Wash (Fig. S7B) siltstones, sandstones and conglomerates dominate the stratigraphy, featuring numerous ice-rafted debris horizons. Sandstone beds typically display normal grading, soft sediment deformation and ripple-cross lamination typical of turbidite successions. Conglomerates are graded and clast-supported, with rounded to sub-angular clasts, and also feature soft sediment deformation indicative of a resedimented origin. These conglomerate horizons are typically conformable with the sandstones and siltstones, although they are locally channelized, and occasionally show broad cross stratification. The predominance of mass flow deposits and laminated marine sediments is indicative of an ice-distal setting. Similarly, in the Southern Kingston Range (Fig. S7C) the most abundant lithofacies present are laminated siltstones, turbiditic sandstones and graded boulder conglomerates, with minor massive diamictite and ice-rafted debris. We interpret the majority of the IFs in the Southern Kingston Range to have been deposited in an ice-distal setting, with some rare horizons associated with diamictites deposited in an ice-proximal setting. The entire glacially influenced succession of the Kingston Peak Formation exceeds ~2800 m in thickness in this area (41, 102), and the IFs exist as discrete, typically thin beds within a ~500 m IF-bearing horizon (41). The IF-bearing Kingston Peak Formation likely accumulated

within actively rifting sub-basins in an ice-distal glaciomarine environment beneath an ice shelf with significant sediment supply (41).

Cryogenian ice sheet dynamics

The geochemical evidence presented here necessitates the explanation of well-oxygenated ice-contact environments and anoxic ice-distal environments on multiple paleocontinents during the Sturtian glaciation. These data may be hypothetically explained by enhanced atmosphere-ocean gas exchange near the grounding line, requiring proximal ice-free oases (sikussaks) with distal ice cover. However, we suggest that the simplest explanation for these data is the proglacial outwash of oxygenated subglacial meltwaters. Understanding the thermal and hydrological regime of the Snowball Earth ice sheets is therefore essential to interpreting the paleoredox state of syn-glacial marine environments.

All three of the studied Sturtian successions are interpreted to have accumulated in a rift basin tectonic setting, which complicates the interpretation of glacial sedimentary processes. There is evidence for synsedimentary tectonism in the study areas of the Yudnamutana Subgroup (29) and the Kingston Peak Formation (41), and in correlative sections in the Chuos Formation (14, 103). However, the glacial hydrology and thermal regime responsible for the deposition of these successions can still be inferred from the sedimentary record. The relative abundance of laminated siltstones and sandstones with ice-rafted debris in many of the measured sections, and the general paucity of glaciofluvial facies, is comparable to glacial successions deposited in modern polar continental shelf glaciomarine environments (47), as opposed to compared to those of temperate or polythermal Arctic fjord settings. Submarine glaciofluvial deposits are present in the Chuos Formation (channelized conglomerates) and Kingston Peak Formation (cross-stratified, channelized sandy gravel deposits with rounded clasts), yet these facies are rare. A sub-ice shelf depositional setting—as indicated by the geochemical data—may also be supported by the interpretation of dropstone-free null zones interpreted in Chuos Formation and Yudnamutana Subgroup successions (104). Therefore, we suggest that the IF-bearing intervals of the Chuos Formation, Yudnamutana Subgroup and Kingston Peak Formation were deposited in settings most analogous to modern Antarctic glaciated margins.

Average global surface temperatures during the Cryogenian glaciations would likely have been much lower than during other ice ages, as inferred by the sedimentological and paleomagnetic evidence for globally distributed ice sheets and equatorial glaciers at sea level (105-107). However, Earth system modelling approaches predict that even under extreme end-member scenarios of global ice coverage, average surface temperatures at low latitudes may have been comparable to those experienced in some modern Antarctic environments (108-110). Paleomagnetic data suggests that all three of the study successions were deposited at low (<30°) paleolatitudes (Fig. 1F) (106, 111), and therefore Antarctic glaciers may present reasonable analogues for Cryogenian low-latitude glaciers. Although much of the Antarctic ice sheet is cold-based, basal ice is near the pressure melting point beneath regions of thick ice and many glaciers are warm based or polythermal (47). Thus, it is feasible that polythermal ice sheets could have been widespread on the low-latitude continental fringes of Rodinia and its fragments during the Cryogenian glaciations. Glacial melting in these settings could be balanced by precipitation on topographic highs (109, 112, 113). Even in models of total ice coverage, locally high rates of sub-ice shelf basal melting are predicted where the upwelling of relatively warm seawater comes into contact with the ice shelf (114).

In Antarctic glaciated margins, much of the sedimentation is deposited by fast-flowing wet-based ice streams feeding ice shelves in an otherwise cold-based ice sheet (115). The angular to subrounded clasts that typify the studied Cryogenian diamictites are consistent with basal transport by a wet-based ice stream (47). Evidence for glaciotectonic shearing and hydrofracturing in Chuos Formation diamictites (54) likely also indicate the presence of basal meltwater (52, 53). Cold-based glacial ice, despite being less erosive, is characterized by debris-rich basal layers due to regelation (47), whereas the basal ice in temperate thermal regimes tends to be debris-poor. Although tectonic mass flows can complicate the interpretation of glaciogenic sedimentation in active rift settings (98), thick packages of glacial sediments considered to be evidence of polythermal regimes are documented in many Cryogenian glacial successions globally (112), including the successions studied here (14, 29, 41, 98). Other evidence from the Cryogenian glacial record for proglacial meltwater outwash from wet-based or polythermal glaciers includes features such as ice

advance and retreat cycles (94, 96, 116, 117) and abundant ice-rafted debris (117-119). As such, Cryogenian glacial successions are consistent with wet-based or polythermal regimes (45, 47, 108, 112, 120-123), with sedimentation actively influenced by an abundant meltwater supply (124, 125).

Significant volumes of subglacial meltwater are drained to the Antarctic seas (77) owing to a widespread and dynamic hydrological system of Antarctica (75). Antarctic subglacial lakes are connected through large subglacial channel networks that maintain a high degree of hydrological connectivity between these reservoirs and coastal discharge (126). This persistent, channelized subglacial drainage system effectively channels meltwater into meltstream exits at the grounding line beneath the Antarctic ice shelves (127). The Antarctic ice sheet is characterized by rapid drainage flood events (jökulhlaups) from subglacial lakes (126) superimposed over a continuous meltwater flux from geothermal and pressure-driven melting (60). Therefore, while the glacial hydrology, thermal regime and meltwater supply of the Cryogenian ice sheets would likely have been variable, we speculate that the depositional environment of the studied successions are supportive of a meltwater supply that fluctuated above a consistent background due to channelized subglacial meltwater outwash and associated sub-ice shelf basal melting. By analogy to modern Antarctic coastlines, we suggest that meltwater outwash would have been concentrated into embayments ~5–15 km wide (60), helping to explain the localized nature of Cryogenian IFs.

Geochemical data interpretation

Fe and Mn geochemistry

Iron enrichment in marine sediments can record important complexities in marine iron cycling. The Fe contents of the Cryogenian IFs do not correlate strongly with any other element analyzed, with the exception of a strong inverse correlation with Si due to the bimodal composition of these sediments (typically <70 % Fe_2O_3+SiO_2). This suggests that the Fe content of the IFs is controlled by the concentration of Fe oxides. To account for detrital Fe input, Fe enrichment is cast in terms of Fe/Al ratios rather than bulk Fe contents (e.g. 5, 128), and the IFs are often orders of magnitude more enriched in Fe than Al. Iron speciation is a tool widely applied to marine sediments as a proxy for paleo-ocean chemistry (129-131). Enrichments of highly reactive Fe in marine sediments are considered to be evidence of anoxic conditions, with the relative proportion of highly reactive Fe present in pyrite used to distinguish between deposition from a euxinic ($H_2S > Fe^{2+}$) or ferruginous ($Fe^{2+} > H_2S$) water column (132). Given that the Fe in the studied IFs is almost exclusively present as hematite and magnetite, and pyrite is virtually absent, these IFs indicate abundant iron scavenging in a ferruginous water column. This seawater Fe(II) could have accumulated under anoxic conditions from several different Fe sources, including hydrothermal venting, ridge volcanism, glacial and continental input, or seafloor alteration. The subsequent oxidation of this Fe(II) led to the precipitation of Fe (oxyhydr)oxides or a Fe-Si gel (e.g. 133), which would have converted to hematite during dehydration and silica release (e.g. 134). The presence of Cryogenian IFs is therefore *prima facie* evidence of anoxic, ferruginous seawater, and the enrichment of Fe oxides is indicative of marine oxidation processes.

The presence of authigenic Mn enrichments in marine sediments can also provide insight into paleoredox conditions. Similar to Fe, dissolved Mn in seawater can be precipitated as Mn-oxides in the presence of O_2 (135), which readily undergo reductive re-dissolution in the presence of Fe(II) (5). The sedimentary enrichment of Mn in the Precambrian geological record has been used to infer a Mn oxide shuttle and therefore marine oxidation (135, 136). As Mn(II) is oxidized at a higher redox potential than Fe(II) (135), we suggest that the ferruginous conditions of the Cryogenian acted as a buffer preventing the enrichment of ice-proximal and ice-distal IFs in Mn-oxides (e.g. 137). Periodic increases in the supply of O_2 could have led to more highly oxidizing conditions in ice-contact settings that could explain the presence of Mn-oxides in these IFs. This interpretation is supported by the presence of manganese formations in other Neoproterozoic glacial successions globally (138, 139).

Cerium anomalies

Unlike most REEs, Ce has two oxidation states and is sensitive to redox processes. Under oxidizing conditions Ce can be efficiently removed from seawater via oxidative scavenging, which is considered to be mediated by Mn–Fe (oxyhydr)oxides, organic ligands, clays and other reactive surfaces (140). This leads to a depletion in Ce in oxic seawater, represented by a negative seawater Ce anomaly ($Ce_n/Ce_n^* < 1$) which can also be preserved in marine chemical sediments (141, 142). As true Ce anomalies can be masked by La anomalies (143), it is necessary to calculate Ce anomalies without utilizing near-neighbors that may also be anomalous. This approach for calculating REE anomalies is discussed in detail in Lawrence et al. (144). As REEY diagrams are plotted on a logarithmic scale, we calculate the UCC-normalized Ce anomaly using a geometric formula:

$$Ce_n/Ce_n^* = Ce_n/(Pr_n \times (Pr_n / Nd_n))$$

The oxidative scavenging of seawater Ce is considered to primarily occur via the sorption of Ce(III) onto precipitating Mn–Fe (oxyhydr)oxide surfaces and the subsequent partial oxidation of Ce(III) to Ce(IV), which effectively decouples Ce from the other trivalent REEs that are in exchange equilibrium with seawater (145, 146). This process depends on the reaction kinetics of Ce(III) oxidation and Ce(IV) desorption, which are relatively slow compared to REEY adsorption and desorption onto Fe (oxyhydr)oxide surfaces (although this reaction may be catalyzed by microbial activity; e.g. 147). Thus, the magnitude and direction of the Ce anomalies preserved in iron oxide-bearing chemical sediments are related to precipitation rates and seawater exposure time (148-150). Cenozoic ferromanganese crusts are characterized by positive Ce anomalies (151-154), which require significant Ce accumulation in order to overcome the pronounced Ce depletion of the surrounding seawater (153). This can be explained by the extremely low accumulation rates (~1–20 mm/Myr) of most modern ferromanganese crusts (152) due to the low Fe concentrations of the modern oceans. By contrast, modern hydrothermal iron oxide-rich sediments have much higher depositional rates (152) and much lower total REE contents than hydrogenetic ferromanganese crusts (151), qualitatively reflecting the REEY profile of their contemporaneous seawater (151, 155, 156) as exchange equilibrium with ambient seawater REEs (other than tetravalent Ce) is reached rapidly (151).

Although the importance Mn oxides in Ce scavenging has long been documented (142, 157), the relative importance of Fe (oxyhydr)oxides in this process is debated. Experimental and geochemical modelling approaches have been used to suggest that the scavenging of Ce via Fe (oxyhydr)oxides is minor at circumneutral conditions (149, 153, 158, 159). The lack of significant positive Ce anomalies in the iron oxide-bearing Cryogenian IFs (and IFs in general) may therefore be explained by their higher depositional rates relative to modern seafloor crusts, a relatively minor influence of Fe (oxyhydr)oxides on Ce scavenging, a pronounced negative Ce anomaly in the water column, or a combination of these factors. Regardless, pure IFs are considered to qualitatively record the REEY composition of their contemporaneous water column (134, 142, 143, 150, 160) when detrital contamination is low, and can therefore be used as a proxy for seawater paleoredox state.

Negative Ce anomalies in IFs are typically interpreted as evidence for iron cycling in oxic seawater (22, 23, 161, 162). True negative Ce anomalies are rare because IF abundance declines following the Great Oxidation Event (163), and several reported cases of negative Ce anomalies in Archean–Paleoproterozoic IFs have been refuted due to issues related to sampling or instrumentation (c.f. 160). The interpretation of negative Ce anomalies in non-skeletal carbonates as evidence of oxic conditions is well established (141, 164, 165), and broadly contemporaneous IFs and carbonates have been shown to record qualitatively similar REE profiles (160, 166) as faithful records of seawater conditions. Thus, following careful screening for detrital contamination and late-stage alteration, negative Ce anomalies in IFs can be used to infer the presence of oxic seawater conditions. Negligible Ce anomalies—characteristic of Archean IFs and carbonates (160, 167)—are considered to indicate anoxic marine conditions (142, 160, 168). Positive Ce anomalies can also occur due to complexities in Ce cycling in a water column with an established redoxcline (160). Settling Mn–Fe (oxyhydr)oxide particles precipitated in oxic surface waters undergo reductive dissolution below the chemocline, releasing Ce into the anoxic waters (141, 169). Subsequent IF deposition

near the redoxcline can therefore preserve this local enrichment, leading to small ($Ce_n/Ce_n^* < \sim 1.3$) positive Ce anomalies in these IFs (160).

Accordingly, the negative Ce anomalies found Cryogenian IFs ($Ce_n/Ce_n^* < 0.62$; mean $Ce_n/Ce_n^* = 0.95$, n = 41) are indicative of oxic Ce cycling at the time of deposition (e.g. 161). These negative Ce anomalies are most commonly found in ice-contact facies IFs, indicating more highly oxidizing conditions in this setting relative to more distal environments. The lack of preservation of negative anomalies in the majority of the ice-proximal and ice-distal facies IFs is likely due to a buffering effect of the dissolved iron reservoir (170). Slight positive Ce anomalies observed in some of the IFs are likely a relic of localized Ce enrichment due to reductive dissolution of Mn oxides in suboxic or anoxic bottom waters. The negligible Ce anomalies that characterize the remainder of the IFs suggest deposition from low O_2 seawater (as suggested for correlative Cryogenian IFs; 171, 172, 173), consistent with the interpretation of widespread anoxia in the syn-glacial Cryogenian oceans. Mn oxides would likely have been the major marine Ce sink in the Cryogenian. Enigmatic, large Cryogenian-aged Mn oxide deposits of uncertain origin have been documented (174-178) and shown to have positive Ce anomalies (174, 175, 179). However, we speculate that the majority of the Mn oxides precipitated in Cryogenian oxygen oases would have generally been diluted by glaciomarine sedimentation, precluding appreciable enrichment.

Compared to bulk digestion methods, *in situ* analyses using LA-ICP-MS allow for micron-scale sample targeting. Using this approach, we were able to minimize detrital contamination and target the primary chemical sedimentary component of samples (i.e. Fe oxides and silica) using a 72 μm spot size. The efficacy of this approach for avoiding detrital contamination is supported by extremely low concentrations of detrital proxy elements such as Al in some analyses (<1 ppm Al). Some degree of silicate contamination is unavoidable in some samples with fine matrix grain size, leading to flatter, shale-like UCC-normalized REEY profiles and higher total REE contents due to detrital REE input. Geochemical cut-offs were implemented to minimize this effect: samples with substantial detrital contamination were excluded from data analysis and discussion. The cut-offs used were aluminum ($Al_2O_3 < 1$ wt %) and total REE content ($\Sigma REE < 50$ ppm), which are both proxies for detrital contamination. The analyses with the highest Al_2O_3 content do not have significant Ce anomalies, and the samples with the most negative and positive Ce anomalies typically have the lowest Al_2O_3, suggesting that the Ce anomalies reflect water column redox cycling and are not controlled by detrital contamination. The REEY composition of IFs is remarkably robust and resistant to alteration and metamorphism (180), making this a reliable proxy for paleo-seawater chemistry. The compatibility of the Ce anomalies with the other redox proxies reinforces the interpretation of paleoredox chemistry based on the geochemistry of these IFs (181).

Iron isotope analysis

Iron isotope fractionations observed in Fe-bearing sediments have variously been interpreted to be the product of partial Fe(II) oxidation due to abiotic redox reactions and biological processes (182-186). The oxidation of aqueous Fe(II) to Fe(III) can lead to strong fractionations and enrich the Fe(III) products in the heavy Fe isotopes by up to ~3–4‰ (187-189). Quantitative Fe(II) oxidation under excess O_2 records the unfractionated Fe isotopic signature of the Fe(II) source (190). However, partial oxidation under low O_2 conditions can lead to the preservation of this fractionation in the rock record. The Fe(II) reservoir in Precambrian ferruginous seawater is considered to have been sourced largely from hydrothermal input and have $\delta^{56}Fe$ values that approximately range from –0.5 to 0‰ (184, 191). The $\delta^{56}Fe$ values of detrital Fe from glacial input is also considered to be ~0‰ (192). Positive $\delta^{56}Fe$ values in IFs have therefore been interpreted as evidence for partial oxidation of Fe(II) in seawater (e.g. 193, 194, 195).

Biological Fe(II) oxidation can also produce similar positive Fe isotope fractionations to the abiotic reaction of Fe(II) with O_2 (196, 197). Biological Fe(II) oxidative mechanisms include anoxygenic photosynthesis with Fe(II) as an electron donor (198, 199), and microbial Fe(II) oxidation coupled to O_2 reduction (200, 201) or nitrate reduction (202). The activity of photosynthethic Fe(II) oxidizing bacteria (185, 193) and chemolithotrophic Fe(II) oxidizing bacteria (195, 203) have both been invoked to explain Fe isotopic trends in Precambrian IFs. The fine lamination the Cryogenian IFs in this study, and the lack of shallow marine sedimentary structures of the host sedimentary strata, suggest deposition below wave base.

Considering also potential ice cover, low light availability likely inhibited photoferrotrophy in these settings (204). The presence of free oxygen could have also precluded photosynthetic Fe(II) oxidation, as anoxygenic photosynthetic bacteria are sensitive to oxygenated environments (205). The intracellular fixation of Fe-rich granules by photosynthetic diatoms has also been documented in modern acid mine drainage environments (206), and analogous iron sequestering photosynthetic biomats have been invoked to explain Cryogenian ironstones in the Chuos Formation (207). It remains unclear whether similar diatoms would have been living in the Cryogenian oceans, and the possible Fe isotope fractionation associated with this intracellular Fe sequestration is unresolved. We suggest that the Fe isotopic signatures and sedimentology of the Cryogenian IFs are most compatible with the non-photosynthetic, partial oxidation of Fe(II). This could have been facilitated by either the abiotic reaction of Fe(II) with O_2 in oxygenated environments, or chemolithotrophic Fe(II) oxidation in microaerobic environments. Partial oxidation by microaerophilic Fe oxidizers was similarly postulated by Halverson et al. (171) as a plausible oxidative mechanism for the Sturtian glacially associated Rapitan IFs. Indeed, wherever Fe(II) and O_2 coexist in modern aqueous environments, chemolithotrophic Fe oxidizing bacteria proliferate (201, 208). These microbes would have likely thrived in Cryogenian glacial environments where meltwaters supplied O_2 into the ferruginous seawater.

Regardless of the exact oxidative pathway, fractionated Fe isotopic compositions in marine chemical sediments are evidence for low seawater oxidizing potential (191), as high O_2 contents lead to quantitative Fe(II) oxidation. To deposit IFs that are extremely enriched in heavy Fe isotopes ($\delta^{56}Fe < 2.70$ ‰), such as the ice-distal Cryogenian IFs (Fig. 2), requires an extremely small degree of oxidation which is difficult to achieve in seawater. Under widespread ice cover due to a floating ice shelf or "sea glacier", gas exchange between the local ice shelf water column and the atmosphere would be inhibited, with a subglacial O_2 supply facilitating partial oxidation. This interpretation is supported by the general agreement of the other independent paleoredox proxies for low-O_2 conditions in the samples characterized by positive Fe isotopic ratios.

Dissimilatory iron reduction (DIR) can produce Fe(II) depleted in heavy isotopes by up to ~3‰ (209, 210), and DIR has been invoked to explain negative $\delta^{56}Fe$ values in IFs and other chemical sediments such as Fe sulfides and Fe carbonates (184, 186, 211, 212). The quantitative oxidation of Fe(II) produced by DIR can lead to isotopically depleted Fe-oxides, and the supply of Fe sourced from DIR of glacially scoured rock flour has been documented in modern Antarctic settings (70). The predominantly positive $\delta^{56}Fe$ values of the Cryogenian IFs suggests that DIR was not a strong influence on the Fe isotopic composition of the Fe(II) source. Although we cannot completely rule out the possibility of a DIR influence on the isotopically light IFs, the combination of the observed trends in Mn enrichment and REEY composition suggests the Fe isotopic trends can be entirely explained by changes in seawater redox state. We suggest that a Rayleigh fractionation model (190, 213) is a simpler and more plausible explanation for the negative $\delta^{56}Fe$ values found in the ice-proximal facies IFs. The long-term removal of $\delta^{56}Fe$-enriched Fe(III) may have resulted in progressive depletion of heavy Fe isotopes in seawater Fe(II) (190, 213), and local quantitative oxidation of ^{56}Fe-depleted seawater Fe(II) resulted in negative $\delta^{56}Fe$ values of IF in ice-contact facies.

In order to draw inferences about paleoredox conditions from Fe isotope studies it is necessary to ensure that the samples analyzed represent a pure chemical sediment that is representative of the paleoenvironmental conditions. Authigenic and diagenetic ferrous Fe phases such as siderite and pyrite can have depleted $\delta^{56}Fe$ values (212, 214, 215) which can potentially act as a mineralogical control on the bulk-rock Fe isotopic composition of IFs. Siderite and pyrite are rare in the Chuos IFs, and nearly absent in the Yudnamutana and Kingston Peak IFs, and these minerals were avoided during sampling and analysis. Detrital Fe contamination from clastic input can also influence the bulk rock Fe isotopic composition. Crustal igneous rocks display a very narrow range of $\delta^{56}Fe$ values, typically ±0.05‰ (182). As such, contamination from detrital Fe can reduce the apparent fractionation of the bulk rock Fe isotopic signature of a chemical sediment. The $\delta^{56}Fe$ isotopic composition of the IFs analyzed shows a weak correlation with Al_2O_3 content, interpreted to be a proxy for detrital contamination of the chemical sediment (170). The highest Al_2O_3 contents tend to have high $\delta^{56}Fe$ values: this trend is difficult to explain via detrital contamination, which should lead to $\delta^{56}Fe$ values closer to 0‰. Similarly, the negative $\delta^{56}Fe$ values have

extremely low Al_2O_3 contents. This suggests that the highly variable, fractionated Fe isotopic signatures of these Cryogenian IFs are unlikely to be related to detrital input. Furthermore, metamorphism cannot readily explain the variability up-section or between different samples from the same outcrop locality (185). The Fe isotope fractionation and variability are instead interpreted to be reliable, primary indicators of redox cycling in the paleo-water column.

Statistical analysis of geochemical data

A range of statistical analyses were employed to test the hypothesis that the ice-contact glaciomarine environment was significantly more oxidizing than the more distal environments, following the approach of Sperling et al. (216). Anderson-Darling tests indicate that the Fe/Al, Mn/Al and Ce anomaly data have strongly skewed distributions, necessitating non-parametric statistical analyses. Analysis of variance (one-way ANOVA and Kruskal-Wallis) methods were used to query whether the generated IF geochemical data from the three different glaciomarine environment bins had a common mean. Pairwise multiple comparisons (Tukey's honest significant difference and Wilcoxon tests) were then used to identify which bins were statistically significant. The results of these analyses (Fig. S10; *SI Appendix* Data S1) show that the ice-contact IF data is significantly different to the ice-proximal and ice-distal IF data for all geochemical proxies. For the Ce anomalies, the post-hoc Tukey's honest significant difference method suggests that the ice-contact and ice-proximal IFs have a common mean. However, a pairwise Wilcoxon test indicates that they are statistically significant ($p = 0.0258$), which should be considered more robust due to the non-normal data distribution of the ice-proximal data. The distributions of the ice-proximal and ice-distal data for the Mn/Al ratios and Ce anomalies are not significantly different. We suggest that these results are a product of the different sensitivities of the paleoredox proxies. Overall, statistical analyses support the hypothesis that the ice-contact environment remained persistently oxidizing.

Cryogenian geobiology

The extreme climate fluctuations of the Cryogenian would have had a drastic effect on the Neoproterozoic biosphere (217, 218), and both mass extinctions (219, 220) and increases in ecological complexity (107, 221-224) have been theorized to have resulted from the Cryogenian glaciations. End member models for total ice cover during Snowball Earth are so severe that they present problems for eukaryotic survival (218, 225-228). Recent advances in paleontology, molecular biology and phylogenetics have added valuable insight into our understanding of the Cryogenian biosphere. Given the drastic effect that the Snowball Earth would have had on the eukaryotic biosphere, it is worthwhile reviewing the evidence from the geological record in order to gain insight into the types of organisms that may have lived in the Cryogenian oceans.

Key eukaryotic lineages diversified during the late Mesoproterozoic to middle Neoproterozoic (229-232), and molecular clock analyses suggest that many of the major eukaryotic clades had evolved prior to the Marinoan, if not the Sturtian, glaciations (233-235). The fossil record supports the evolution of the Archaeplastida, Opisthokonta and Amoebozoa prior to the Cryogenian, as fossils plausibly interpreted as fungi (236), red algae (237, 238), green algae (239) and arcellinid testate amoebae (240-242) predate the Cryogenian Period. The diverse vase-shaped microfossils from the Tonian Period generally interpreted as arcellinid testate amoebae (Amoebozoa; 240, 241) have also been previously compared to modern euglyphid testate amoebae (i.e. Rhizaria; 243), although this interpretation has recently fallen out of favor (244, 245). Other enigmatic protistan forms reported from Tonian and Cryogenian strata have been tentatively interpreted as foraminifera (246), ciliates (247, 248), and other forms of arcellinid testate amoebae (248, 249). Cryogenian macrofossils have also been interpreted as algae (250). The geochemical and biomarker record suggests that eukaryotes became the dominant primary producers during this time (224, 251). Fossil evidence for enigmatic, complex eukaryotic macrofossils (252) and biological innovations such as cell differentiation (253); biomineralization (254); heterocysts (255); and eukaryovory (256) clearly demonstrates increasing ecosystem complexity in the early Neoproterozoic.

Many molecular clocks estimate that the divergence of animals occurred during the Tonian or Cryogenian (233, 257, 258). No unequivocal metazoan fossils have been identified in Cryogenian or older

strata. Bilaterian fossils from ca. 560 Ma strata (259, 260) and associated cholesteroid biomarkers (261) therefore provide the oldest widely accepted direct evidence for animal life. However, rare candidates for Cryogenian animal fossils have been proposed. These include macroscopic discoidal structures in the Cryogenian postglacial strata of northwestern Canada (262). Although the affinity of these fossils is uncertain, the so-called "Twitya discs" have been interpreted to represent stem-group cnidarians (262), or the holdfast structures of rangeomorphs (263) or their primitive ancestors (264). Alternatively, these discoidal structures may simply represent fossil colonial microbes (265) or abiological sedimentary structures. Sponge body fossils have been interpreted in Tonian and Cryogenian strata (266-268), however, these interpretations are controversial and have received little support (269-271).

Other purported evidence supporting the existence of animals in the Cryogenian comes from the biomarker record. Cryogenian-aged rocks from Oman, interpreted to have been deposited between the Sturtian and Marinoan glaciations, contain the fossilized remains of sterols that in modern ecosystems are produced in abundance by demosponges (272, 273). Given that demosponges are a derived clade of the Porifera, these findings have been suggested to imply that sponges had evolved by the Cryogenian and likely survived in marine environments during the Sturtian glaciation (260, 272). However, ambiguity in the age of these Cryogenian biomarkers remains, and given that they pre-date the oldest unequivocal fossil evidence for demosponges by ca. 100 Ma, their significance is uncertain (274). Furthermore, precursors molecules to these steranes can also be produced by unicellular rhizarians questioning the efficacy of these steranes as sponge biomarkers (275). It should be noted that rhizarians are near-exclusively obligate aerobes, and thus their survival in the Cryogenian syn-glacial oceans may also necessitate oxic habitats, although the pre-Cryogenian fossil record of rhizarians is also ambiguous. Another, more enigmatic sterane biomarker of unknown origin known as "cryostane" found in pre-Sturtian rocks lends some support to the interpreted presence of sponges in the Cryogenian (276). In summary, the presence or absence of sponges in Cryogenian oceans remains speculative (see a recent review by Botting and Muir, 277). If sponges (or their 'proto-sponge' ancestors) inhabited glaciomarine environments during the Sturtian glaciation, they would have had over 50 Ma to gradually expand their habitat closer to meltwater outwash sites, which may have been an important adaptation for the survival of the post-glacial freshwater influx.

Although the Cryogenian fossil record is much sparser and more difficult to interpret than that of later periods, studies of Neoproterozoic fossil assemblages permit tests of hypotheses on eukaryotic evolution (229, 278-283), with implications for understanding Cryogenian climate and oxygen dynamics. The Cryogenian eukaryotic fossil record predominantly consists of acritarchs, and studies have shown a decrease in diversity of eukaryotic fossil assemblages around the middle Neoproterozoic (278, 281, 284, 285), with a particularly low eukaryotic diversity during the Cryogenian (283). This has been speculated to represent an extinction event caused by Cryogenian glaciation (284-286). However, high-resolution paleontological studies coupled with greater geochronological constraints have demonstrated that this decline in eukaryotic diversity predates the onset of the Sturtian glaciation (281, 282, 287). The survival of several eukaryotic taxa throughout the Cryogenian and into the Ediacaran (226, 288, 289) has been used to argue for substantial aerobic habitats during the Cryogenian glaciations (226).

Links between glaciation and oxygenation

Cryosphere activity is an important control on the redox state of the modern oceans. The seawater of modern glaciomarine environments comprises a mixture of warm circumpolar deep water, cold dense water resulting from brine-rejection during sea ice formation, and ice shelf water supplied by glacial ice melting (290). Dense shelf water plays a key role in ventilating the deep oceans (291), yet glacial meltwater also forms a significant seawater constituent of modern glaciated margins (60, 61). The solubility of oxygen in seawater is inversely proportional to temperature (292, 293), and glacial meltwaters can be enriched in oxygen due to the dissolution of gas bubbles trapped in glacial ice (64, 67, 294, 295). Because modern shallow marine environments are pervasively oxygenated, the delivery of O_2 to modern glaciomarine environments via glacial meltwater has received little attention (67, 290) compared to the production of sea ice brines. Given the observation of oxygenated subglacial and supraglacial meltwaters in modern polar environments (64, 295), we suggest that a glacial oxygen supply was active in previous glaciations, albeit

potentially limited by the availability of O_2. Although the timing of the origin of oxygenic photosynthesis is contentious, oxygenic photosynthesis undoubtedly predates the Great Oxidation Event (296, 297), and there is geochemical evidence that suggests that biological O_2 production may have been active by the Mesoarchean (298). Glacial delivery of atmospheric O_2 to marine environments could hypothetically have occurred in any glaciation following this evolutionary advent. Despite a dearth of absolute geochronological constraints on many aspects of the Precambrian geological record, there appears to be a temporal association between major ice ages and the oxidation of the Earth's surface environments (222, 299-303). We argue that the transfer of atmospheric O_2 to the oceans via proglacial outwash of subglacial meltwater is a simple mechanism that should be considered when interpreting marine redox shifts during glaciation.

The Neoproterozoic Era experienced at least three extreme glaciations: the Sturtian and Marinoan glaciations of the Cryogenian Period, and the Gaskiers glaciation of the Ediacaran Period (109, 220). Although anoxic marine environments likely persisted into the Phanerozoic (164, 216), there is abundant evidence from geochemical proxies used to argue for increases in marine oxygenation following glaciation in the Cryogenian (172, 301, 304-306) and Ediacaran (307-309). Authigenic Fe and Mn enrichment is ubiquitous in Neoproterozoic glacial successions. Although the geochronology and stratigraphic correlation of many Neoproterozoic glacial successions remains ambiguous, IFs correlated to the Sturtian glaciation are global in distribution. These deposits can be found in the USA (310-312); Canada (313); China (314); Australia (315); South Africa (316); and Namibia (317). The Sturtian glacially associated IFs of Namibia also contain abundant manganese formations (138). While it has been argued that Neoproterozoic IFs are restricted to Sturtian glacial successions (316, 318), other Neoproterozoic IFs of uncertain age are reported from Mongolia (319); Kyrgyzstan (320); Russia (320, 321); Iran (322); Egypt and Saudi Arabia (323); Morocco (324); Togo (325); Uruguay (326); Bolivia (327); and Brazil (328), warranting further investigation. The Fe and Mn formations of Bolivia, Brazil (329) and Togo (330) have been correlated to the Marinoan glaciation, and many Marinoan glacial diamictites have an Fe-rich matrix (30). Geochronological constrains also permit tentative correlation of deposits in Brazil (161, 177), Uruguay (331) and Iran (332) to the Ediacaran Gaskiers glaciation.

Although some authors favor rift-related hydrothermal-exhalative (92, 333-335) or volcanogenic (336, 337) models, the association of Cryogenian IFs with glacial deposits has led to the hypothesis that these deposits are the product of marine redox processes and genetically linked to glaciation (139, 338). Most commonly, glaciation is linked to heightened marine anoxia and elevated dissolved Fe concentrations. Syn-glacial eustatic sea level fall has been suggested to have inhibited ocean circulation (339); concentrated marine solutes (340); reduced riverine sulfate supply (341); and elevated the Fe flux from the weathering of glacially eroded bedrock (342) and hydrothermal input from depressurized ridge systems (343). Alternatively, enhanced Fe delivery may have been sourced from the weathering of continental flood basalts (173, 344, 345) or rift-related hydrothermalism (346). Widespread oceanic ice cover during Cryogenian glaciation (219, 220, 338), or localized ice cover over restricted basins (139, 347), has also been invoked as a causal mechanism for the development of ferruginous conditions (123, 219, 338). Subsequent glacial retreat would lead to the re-coupling of the oceans and the oxygenated atmosphere. Alternatively, Kaufman et al. (348) suggested that prolonged Proterozoic ocean stratification promoted the development of ferruginous deep waters, and that Cryogenian syn-glacial upwelling of ferruginous seawater into oxygenated surface waters may have been responsible for IF deposition. Halverson et al. (171) proposed that the seasonal upwelling of ferruginous seawaters—enriched in Fe(II) from seafloor alteration and the weathering of continental flood basalts (349)—across a stratified chemocline into oxic surface waters could have led to the deposition of IF.

Several authors have proposed a genetic relationship between various forms of glacial meltwater and IF deposition. For the Paleoproterozoic Snowball Earth events, the accumulation of atmospheric hydrogen peroxide during glaciation, and the subsequent transfer to the marine environment via basal ice shelf melting, has been invoked as an oxidative mechanism (350, 351). Yeo (100) presented a model for Cryogenian IF whereby Fe(II)-rich hydrothermal plumes were displaced by cold, dense glacial fluids leading to IFs intercalated with glacial deposits. This model was supported by later studies of Cryogenian IFs (352, 353). Alternatively, Urban et al. (139) proposed that proglacial meltwater outwash could have

transported ferruginous seawater out from anoxic, ice covered fjords and into the oxygenated open marine environment, depositing Fe- and Mn-oxides. Hurrey (339) postulated that the glacial meltwater itself may have been oxygenated and therefore capable of oxidizing the ferruginous Cryogenian seawater, a possibility also raised by Hoffman (354) and Halverson et al. (171).

The precipitation of abundant Fe-oxides requires a strong redox gradient and high seawater Fe(II) concentrations, both of which would likely have been exacerbated during the intense Sturtian glaciation. Therefore, while Sturtian IFs are indicative of seawater oxidative processes, glacial meltwater O_2 supply was likely active during other glaciations throughout Earth history when the unique conditions for IF deposition and preservation were not met. The weathering of late Tonian continental flood basalts (344, 349) and extensive shallow ridge volcanism during the rifting of Rodinia (355) have both been suggested to have enhanced delivery of Fe in the leadup to the Sturtian glaciation. Modelling of the oxygen dynamics of a Snowball Earth event predicts a decline in the Fe(II) concentrations of the oceanic reservoir following deglaciation (299). The multi-million-year oxidation of seawater via the outwash of subglacial meltwater would have also acted to lower seawater Fe(II) concentrations during the Sturtian, as evidenced by the removal and subsequent of seawater Fe(II) burial as Fe oxides in IFs. Therefore, while the oceans remained dominantly ferruginous during the Marinoan glaciation (131), syn-glacial seawater may have had insufficient Fe(II) concentrations for IF deposition. Differences in glacial thermal regime and hydrology may have also led to a different ratio of glacial sedimentation authigenic Fe oxidation in glaciomarine environments during the Marinoan. Alternatively, the Marinoan glaciation may not have been sufficiently lengthy for this process to leave a lasting mark on the stratigraphic record, particularly as ice-contact glaciomarine settings have low preservation potential. Further study of the distribution of sedimentary Fe in Marinoan glacial sediments may help to resolve this problem. Variations in glacial sedimentation rates, seawater Fe(II) concentrations and ice sheet dynamism may explain the episodic nature of IF within Sturtian glacial successions. Overall, the O_2 contents of the atmosphere, oceans and meltwaters were likely the strongest control on syn-glacial IF deposition. Further improvements in our understanding of Cryogenian atmospheric O_2 contents, marine Fe(II) concentrations and subglacial meltwater fluxes will improve our understanding of this glacial oxygen pump, and numerical modelling approaches may help to resolve the temporal and spatial extent of these syn-glacial marine oxygen oases.

Fig. S1.

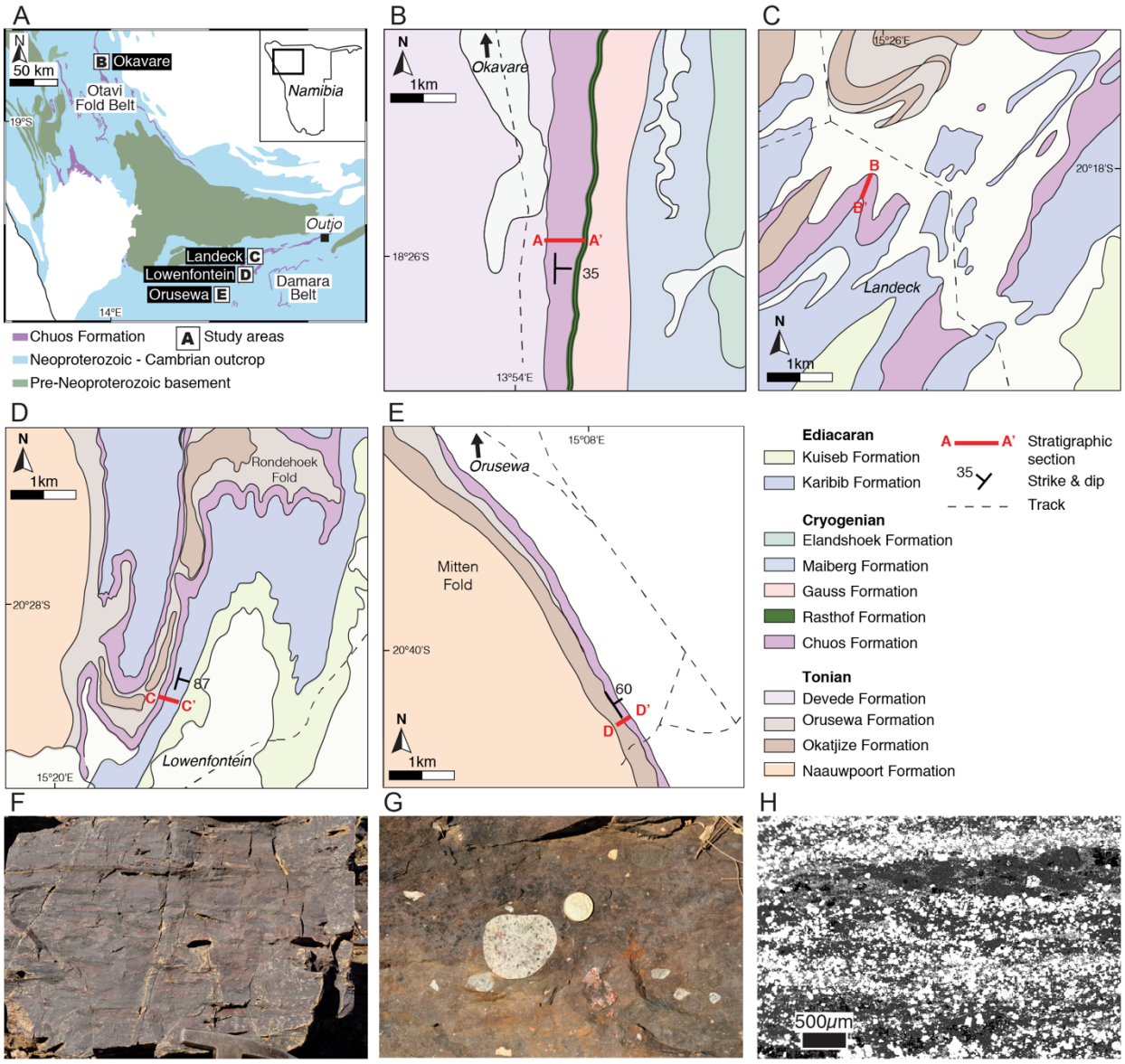

Chuos Formation in the Kunene Region of north-western Namibia. (**A**) Locality map of the study areas. Geological maps of the study areas (**B**) at Okavare in the Otavi Fold Belt; (**C**) at Landeck south of Fransfontein Ridge; (**D**) at Lowenfontein, Rondehoek Fold; and (**E**) at Mitten Fold near Orusewa in the Damara Belt. Stratigraphic section A-A' is shown in Fig. S2; B-B', C-C' and D-D' are shown in Fig. S3. (**F**) Bedded cherty IF at Landeck. (**G**) Massive ferruginous diamictite containing outsized, extrabasinal clasts of heterogeneous lithologies, Okavare. (**H**) Scanning electron microscope (SEM) image of the Chuos IF from Okavare, featuring laminations of coarse magnetite (white) and hematite (light grey) within a matrix of quartz (dark grey) with minor dolomite and clay minerals.

Fig. S2.

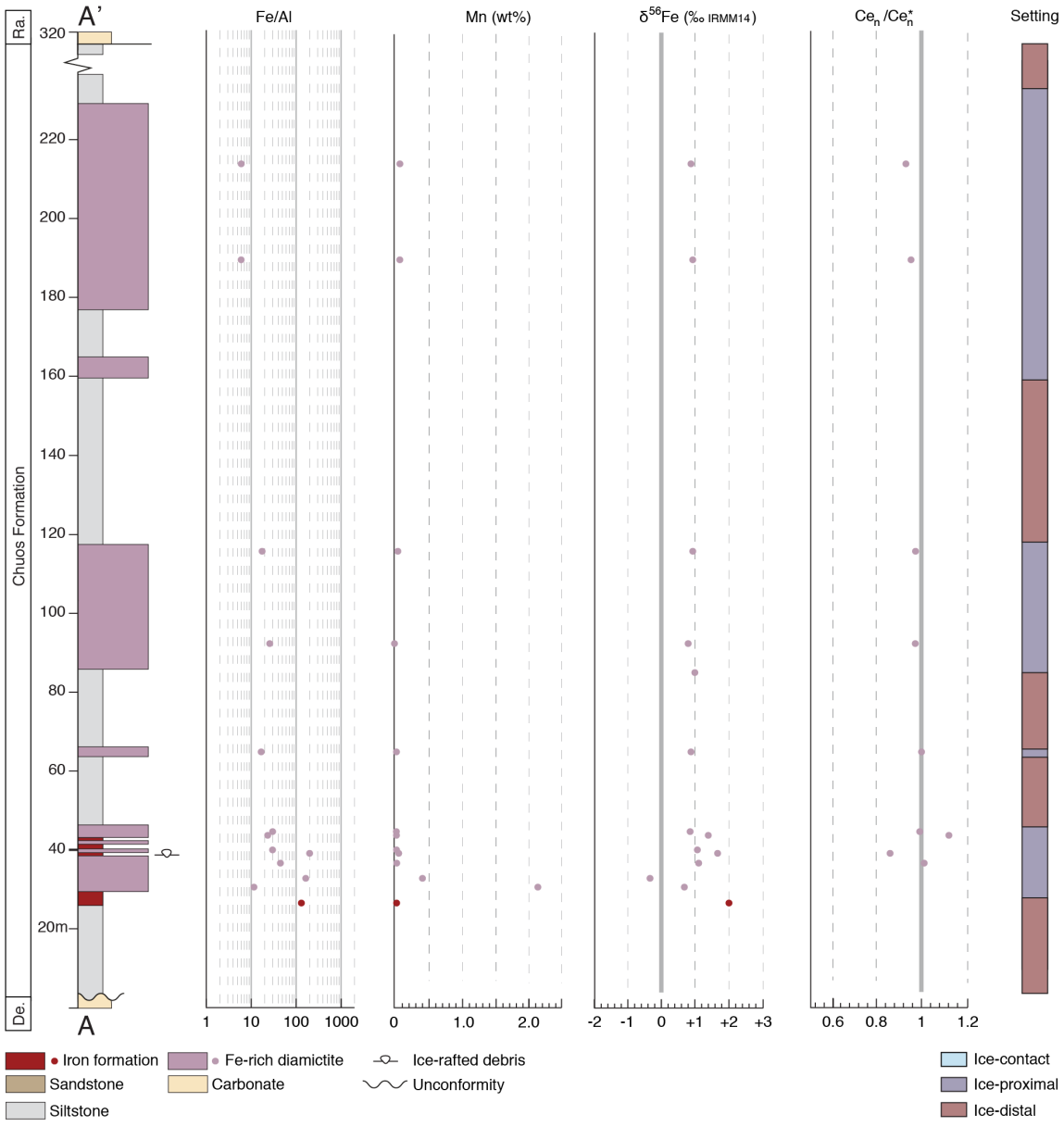

Chemostratigraphy of the Chuos Formation at Okavare in the Otavi Fold Belt, Namibia. Location (A-A') shown in Fig. S1B. Geochemical data showing the stratigraphic changes in Fe/Al ratios, Mn content, Fe isotope composition ($\delta^{56}Fe$) and mean Ce anomalies (Ce_n/Ce_n^*) for the IF horizons of the Chuos Formation. The interpreted glaciomarine depositional setting is highlighted. The ferruginous matrix of some Fe-rich diamictites were also analyzed; these data are shown for comparison. Note that in order to select the best-preserved rocks, several IF samples were taken from adjacent to the measured section and are therefore not plotted on this stratigraphic diagram (see Data S1). Abbreviations: De. = Devede Formation, Ra. = Rasthof Formation.

Fig. S3.

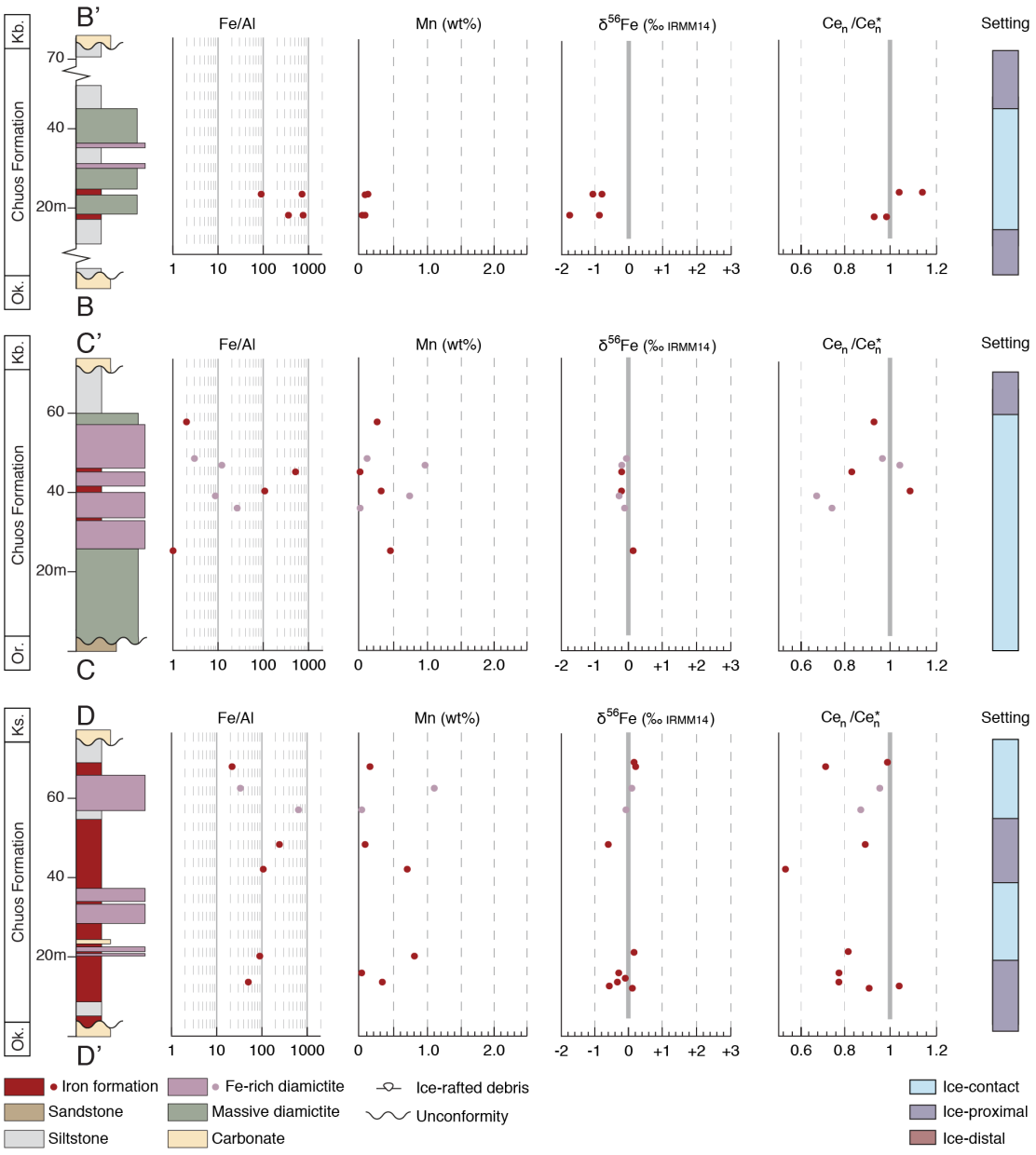

Chemostratigraphy of the Chuos Formation in the Damara Belt, Namibia. Sections were measured at Landeck (B-B'), Rondehoek Fold (C-C') and Mitten Fold (D-D'); locations shown in Fig. S1C-E. Geochemical data showing the stratigraphic changes in Fe/Al ratios, Mn content, Fe isotope composition ($\delta^{56}Fe$) and mean Ce anomalies (Ce_n/Ce_n^*) for the IF horizons of the Chuos Formation. The interpreted glaciomarine depositional setting is highlighted. The ferruginous matrix of some Fe-rich diamictites were also analyzed; these data are shown for comparison. Note that some samples were taken from adjacent to measured sections and are therefore not plotted on stratigraphic diagrams. Abbreviations: Ok. = Okatjize Formation, Ks. = Kuiseb Formation, Or = Orusewa Formation, Kb. = Karibib Formation.

Fig. S4.

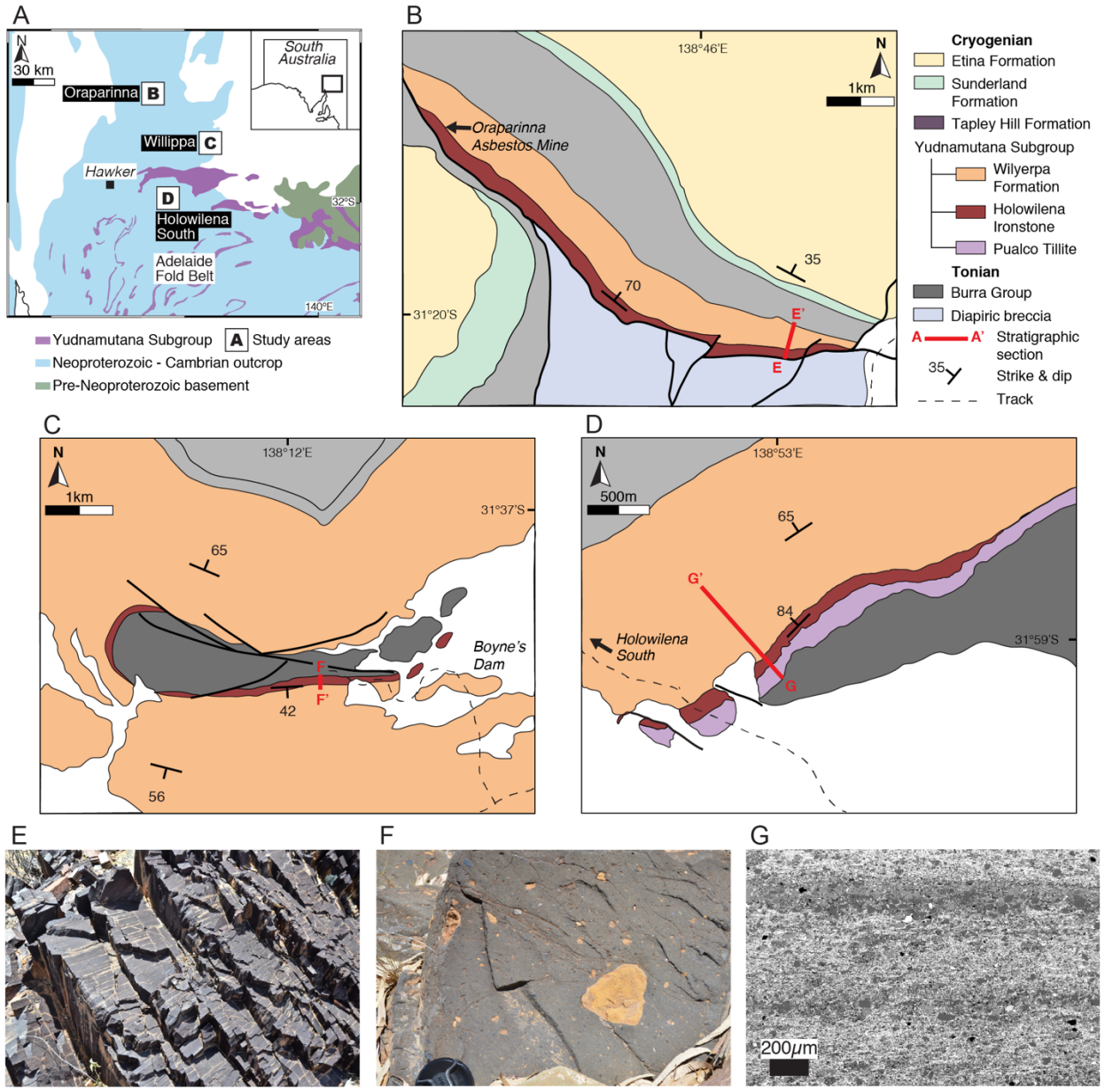

The Yudnamutana Subgroup within the Adelaide Fold Belt, South Australia. (**A**) Locality map of the study areas. Geological maps of the study areas (**B**) at Oraparinna in the Ikara-Flinders Ranges; (**C**): at Willippa, east of Hawker and (**D**): at Holowilena South, east of Craddock. Stratigraphic section E-E' is shown in Fig. S5; F-F' and G-G' are shown in Fig. S6. (**E**) Thick (>10 m) succession of finely laminated IF, Holowilena South. (**F**) Massive, ferruginous diamictite containing outsized clasts, Holowilena South. (**G**) SEM image of the Holowilena Ironstone featuring finely laminated hematite (white), with quartz grains and a chert matrix (grey).

Fig. S5.

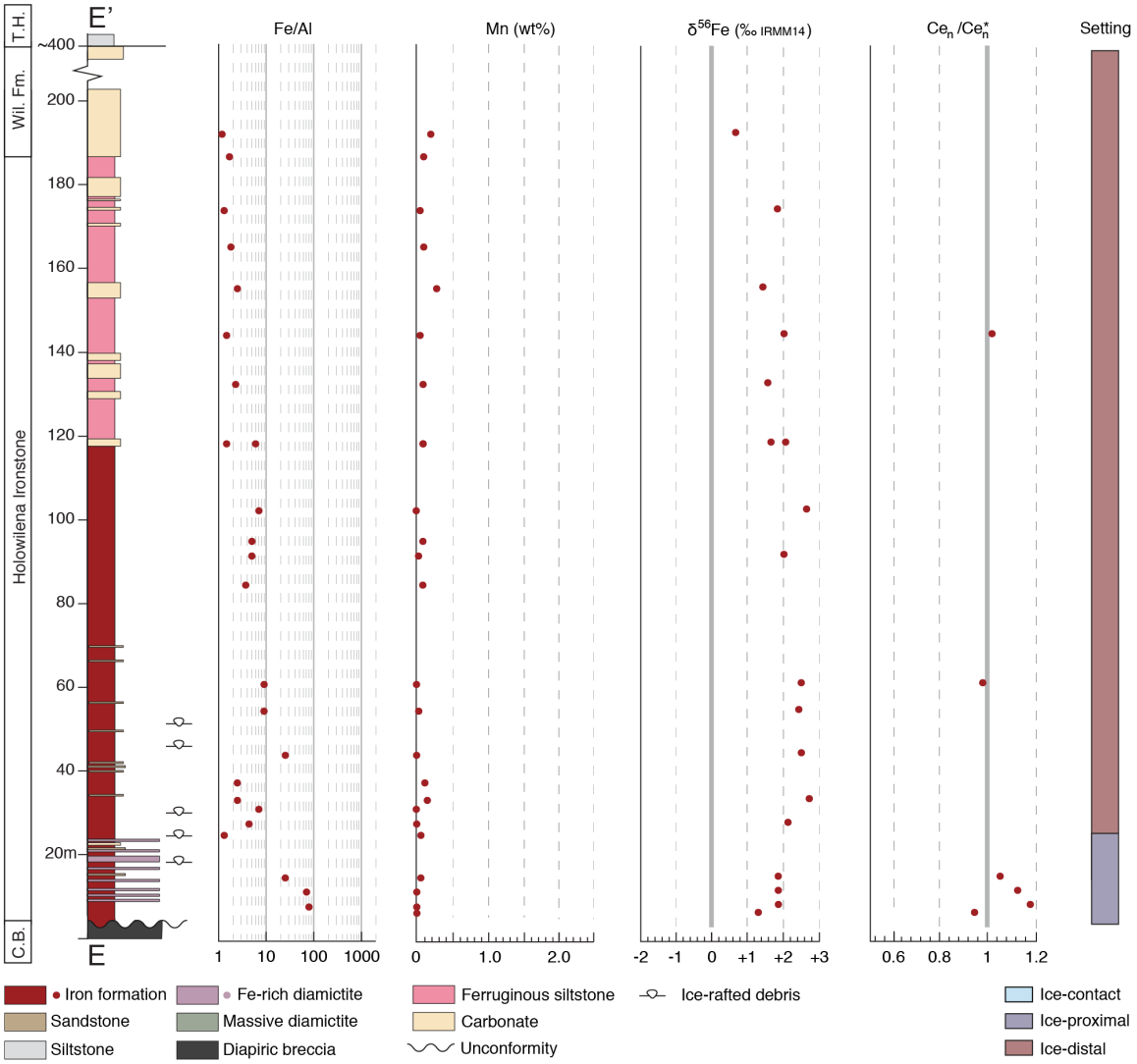

Chemostratigraphy of the Holowilena Ironstone (Yudnamutana Subgroup) at Oraparinna, South Australia. Location shown in Figure S4D (E-E'). Geochemical data showing the stratigraphic changes in Fe/Al ratios, Mn content, Fe isotope composition ($\delta^{56}Fe$) and mean Ce anomalies (Ce_n/Ce_n^*) for the IF horizons and ferruginous siltstones of the Holowilena Ironstone. The interpreted glaciomarine depositional setting is highlighted. Abbreviations: C.B. = Callanna Beds, Wil. Fm = Wilyerpa Formation, T.H. = Tapley Hill Formation.

Fig. S6.

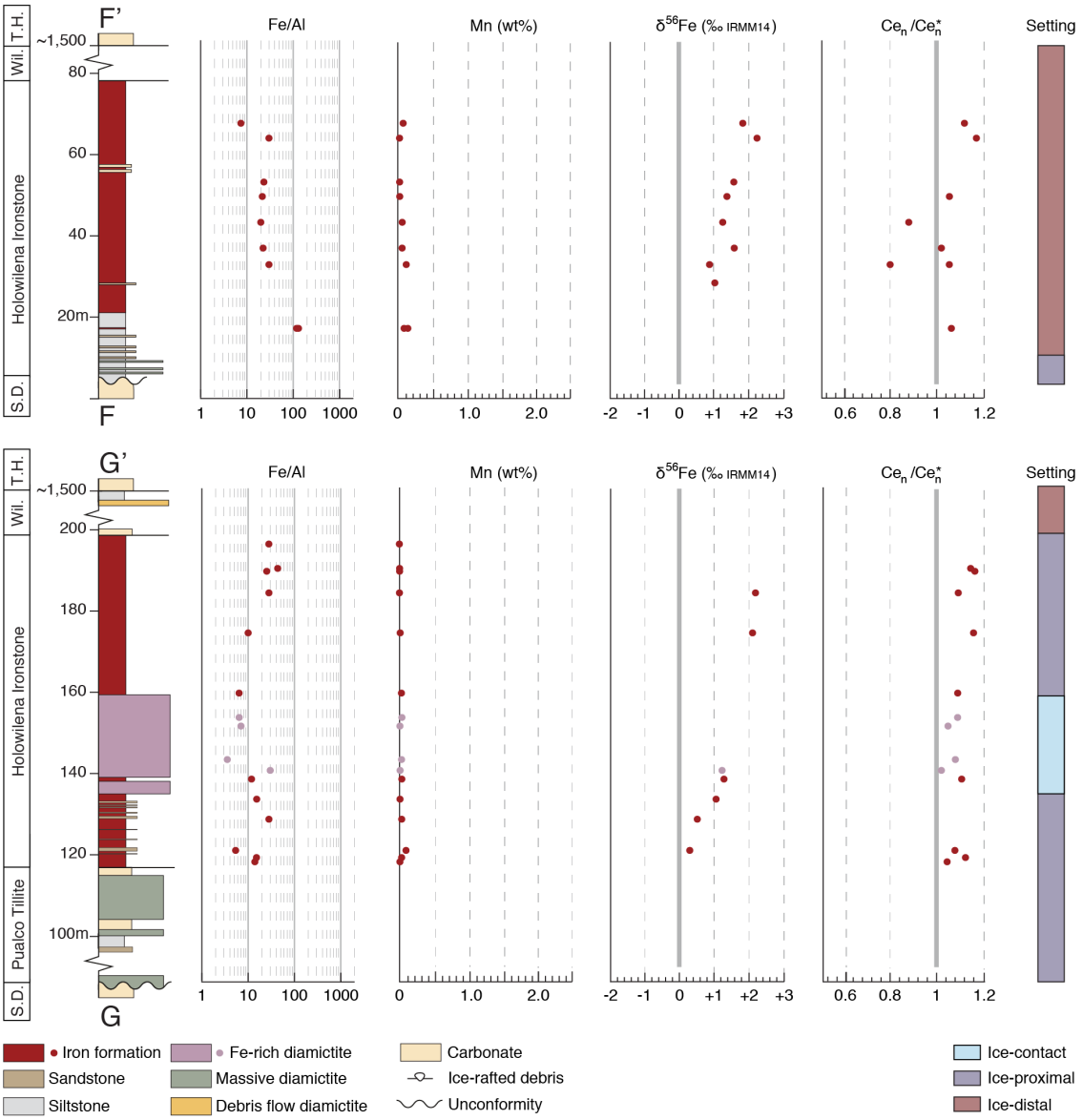

Chemostratigraphy of the Holowilena Ironstone (Yudnamutana Subgroup) in the central Adelaide Fold Belt, South Australia. Sections were measured at Willippa (F-F') and Holowilena South (G-G'); locations shown in Fig. S4B-C. Geochemical data showing the stratigraphic changes in Fe/Al ratios, Mn content, Fe isotope composition ($\delta^{56}Fe$) and mean Ce anomalies (Ce_n/Ce_n^*) for the IF horizons of the Holowilena Ironstone. The interpreted glaciomarine depositional setting is highlighted. The ferruginous matrix of some Fe-rich diamictites were also analyzed; these data are shown for comparison. Abbreviations: S.D. = Skillogalee Dolomite (Burra Group), Wil. = Wilyerpa Formation, T.H. = Tapley Hill Formation.

Fig. S7.

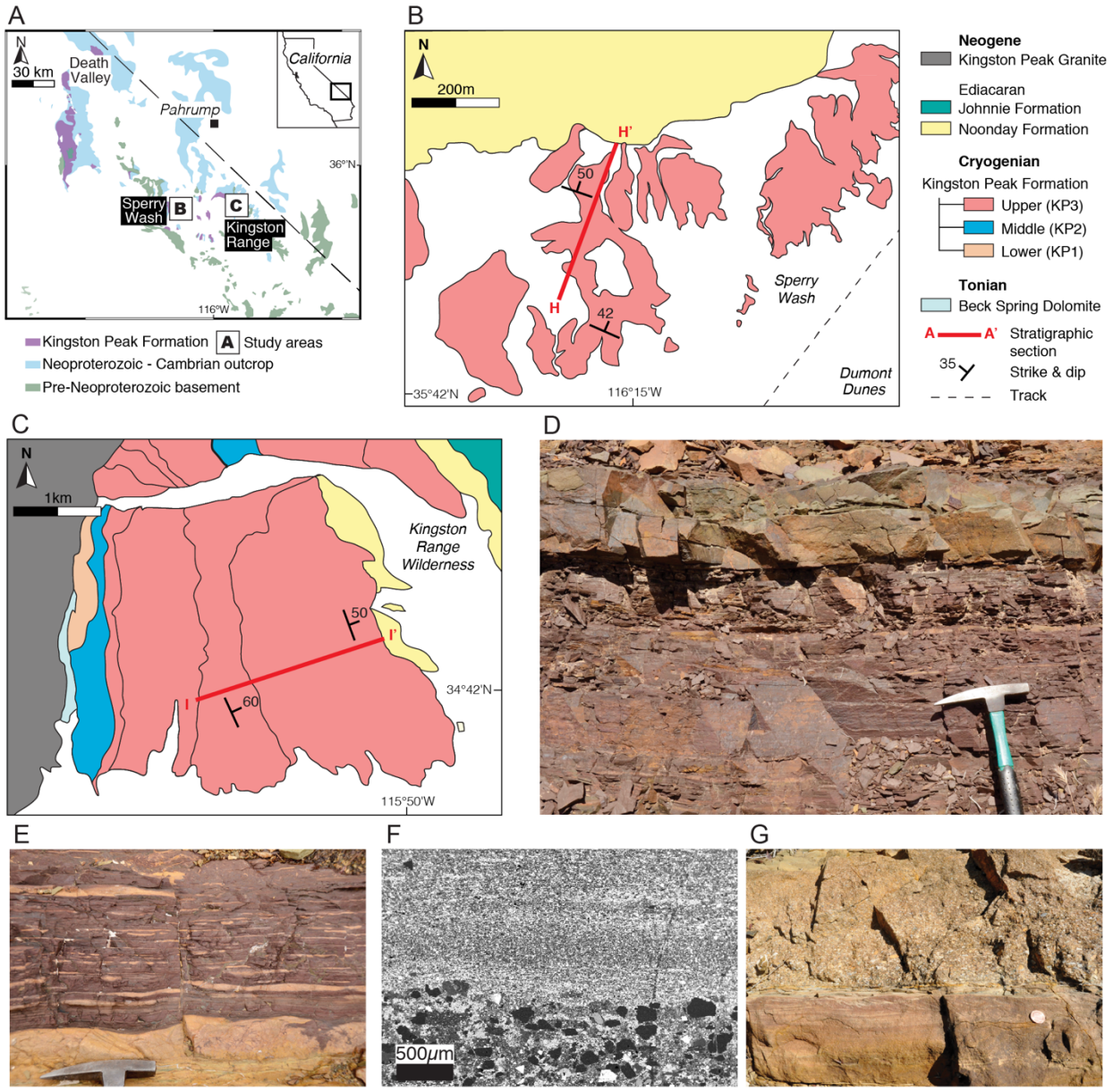

The Kingston Peak Formation in south-eastern Death Valley and the Kingston Range Wilderness, California, USA. (**A**) Locality map of the study areas. Geological maps of (**B**) Sperry Wash near the Dumont Dunes (99) and (**C**) the southern Kingston Range (356). Stratigraphic sections H-H' and I-I' are shown in Fig. S8. (**D**) Finely laminated iron formation overlain by sandstone, Kingston Range Wilderness. (**E**) Sandstone lenses featuring load structures within iron formation, Kingston Range Wilderness. (**F**) SEM image of a sandstone interbed overlain by finely laminated hematite (white) with a chert matrix. (**G**) Coarse gravel conglomerate displaying prominent grading overlying graded sandstone with cross lamination, interpreted to represent mass flow deposits.

Fig. S8.

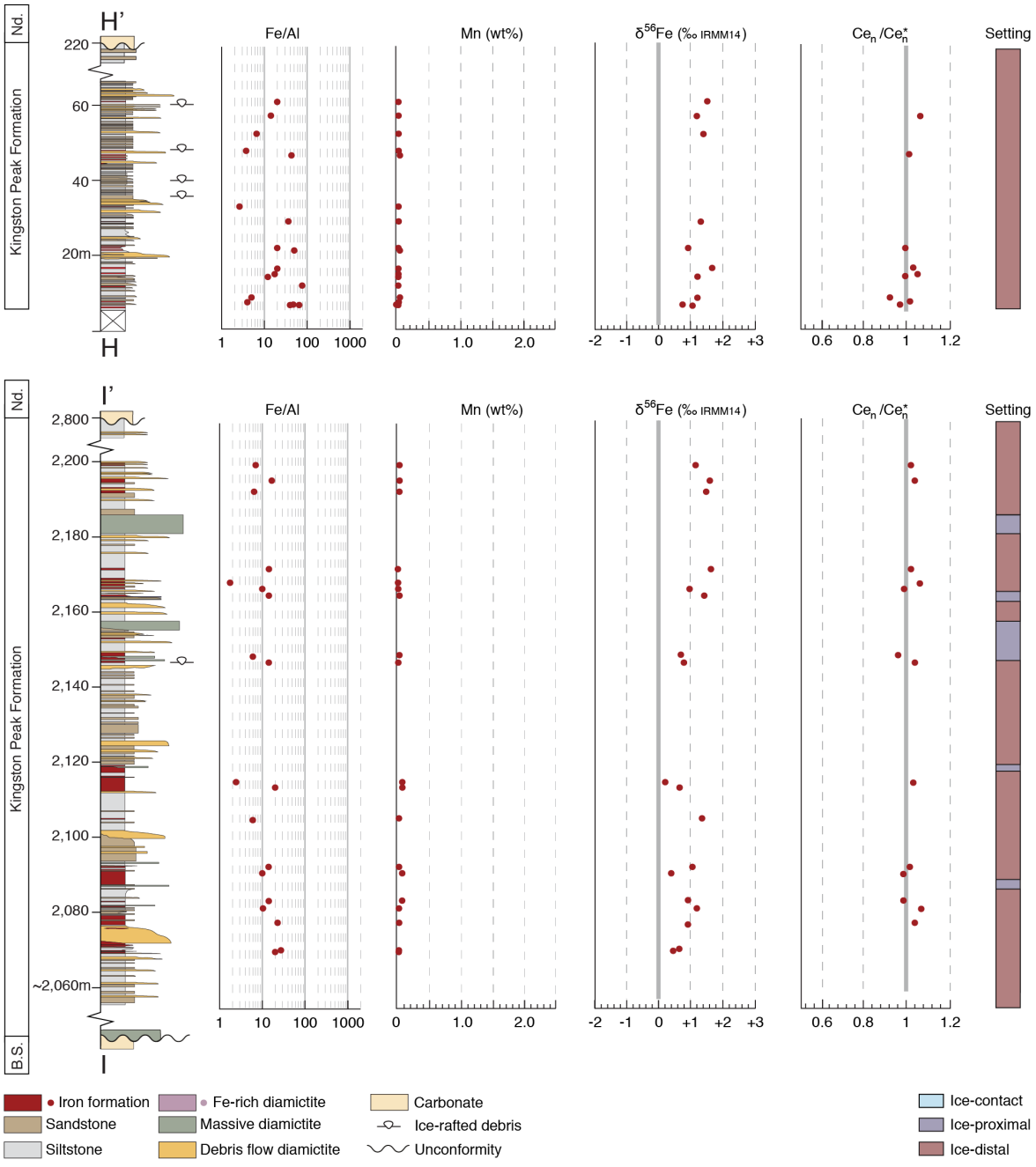

Chemostratigraphy of the iron formation-bearing intervals of the Kingston Peak Formation, California. Sections were measured at Sperry Wash (H-H') and the southern Kingston Range Wilderness (I-I'); locations shown in Fig. S7B-C. Geochemical data showing the stratigraphic changes in Fe/Al ratios, Mn content, Fe isotope composition ($\delta^{56}Fe$) and mean Ce anomalies (Ce_n/Ce_n^*) for the iron formation horizons of the Kingston Peak Formation. The interpreted glaciomarine depositional setting is highlighted. Abbreviations: B.S. = Beck Spring Dolomite, Nd. = Noonday Formation.

Fig. S9.

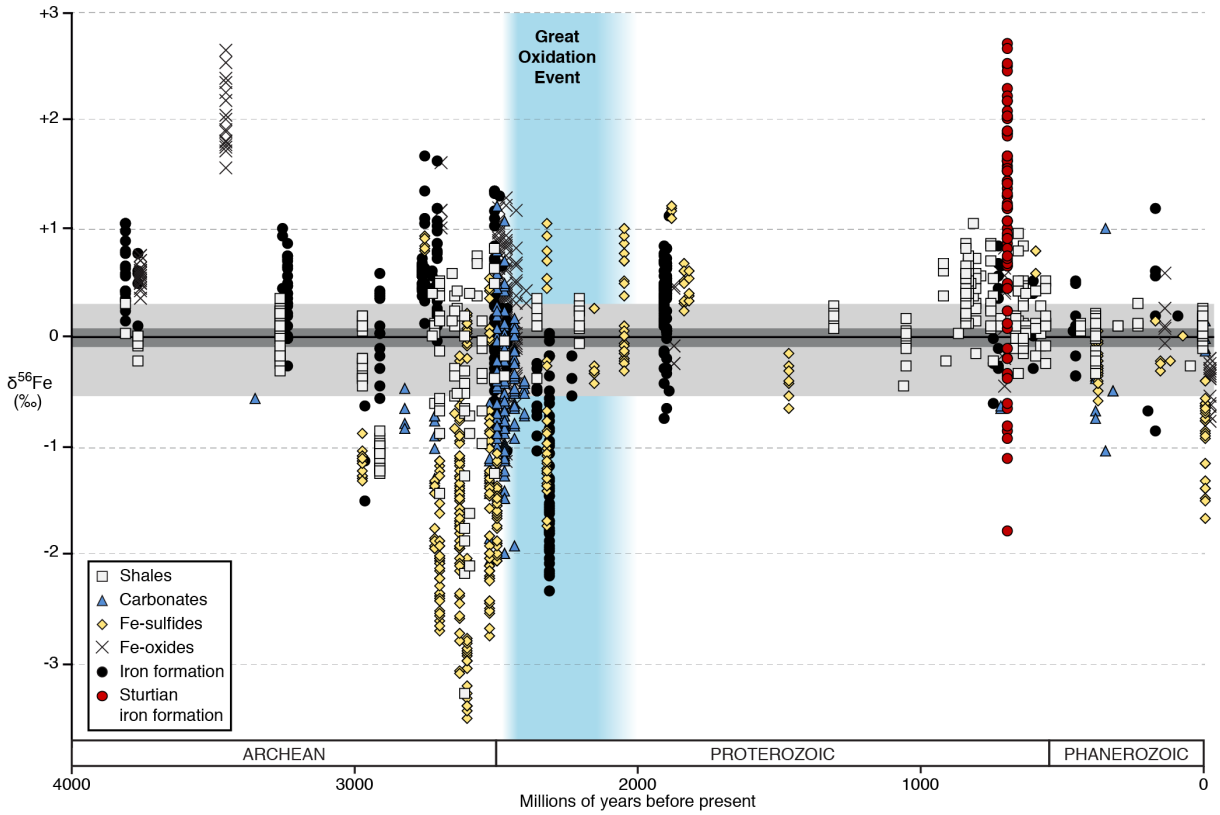

Variation in sedimentary Fe isotopic ratios throughout Earth's history. The Fe isotope compositions of Cryogenian iron formations (red circles; this study) are highlighted relative to other sedimentary Fe-bearing phases from published literature. The dark grey and light grey horizontal bars represent the range of δ^{56}Fe values for igneous rocks and hydrothermal Fe(II) sources respectively (5, 190, 357). The blue vertical bar represents the broad range of the Great Oxidation Event (297). Figure based upon the compilations of Bekker et al. (358), Busigny et al. (5) and McCoy et al. (359), updated with new results and additional literature data (193, 360-366).

Fig. S10.

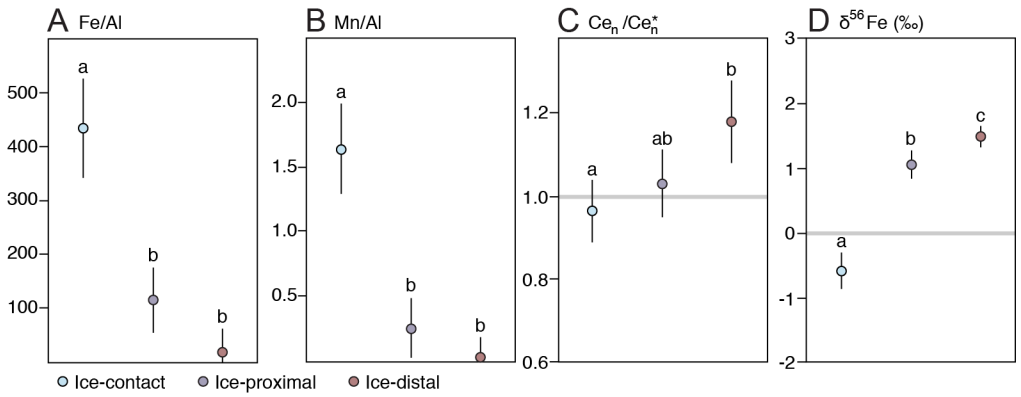

Statistical comparisons of Sturtian IF paleoredox proxy data: (**A**) Fe/Al ratios; (**B**) Mn/Al ratios; (**C**) Ce anomalies (Ce_n/Ce_n*****); and (**D**) Fe isotope ratios ($\delta^{56}Fe$) binned according to their interpreted depositional environment (ice-contact, ice-proximal or ice-distal). The circles represent the mean of the samples for each glaciomarine environment, and the whiskers represent the standard error. The letters (a, b or c) represent the results of multiple comparisons using Tukey's honest significant difference test performed following analysis of variance: bins annotated with the same letter are not significantly different. The ice-contact facies IFs are significantly different to the ice-proximal facies IFs in all cases except for Ce anomalies, and significantly different from the ice-distal facies IFs in all cases.

Table S1.

Facies	Predominant process interpretation	Glaciomarine depositional environment
Mudstone	Hemipelagic suspension settling	Open marine to ice-distal, with or without ice-rafting
Interbedded mudstone and sandstone	Low to moderate density sediment gravity flow Marine outwash resedimentation Hemipelagic suspension settling with ice-rafted debris	Ice-distal Grounding line fan
Mudstone with outsized clasts	Subglacial deposition Hemipelagic suspension settling Ice-rafted debris rainout	Ice-proximal to ice-distal
Rhythmically interbedded mudstone with siltstone or sandstone	Suspension settling from turbid plumes Low-density turbidity current deposition Ice-rafted debris rainout	Ice-proximal to ice-distal
Sandstone Sandy gravel with subrounded clasts	Sediment gravity flows Glaciofluvial outwash	Ice-proximal Grounding line fan
Conglomerate	Marine outwash resedimentation Mass flow resedimentation	Ice-proximal Grounding line fan
Breccia	Mass flow resedimentation Volcanogenic debris flow	Ice-proximal Grounding line
Stratified diamictite	Subglacial deposition Ice-rafted debris rainout with currents Debris flow deposition	Ice-contact to ice-proximal
Massive diamictite	Subglacial deposition Ice-rafted debris rainout without currents Debris flow deposition	Ice-contact to ice-proximal

Interpretation of the depositional processes responsible for the various sedimentary facies observed in Sturtian glacial successions, and their assigned glaciomarine depositional environment. Adapted from Naish et al. (48).

Data S1. (separate file)

In situ geochemical data; bulk rock geochemical data; bulk rock Fe isotope geochemical data; results of statistical analyses of iron formation geochemical data.

References for SI reference citations

1. C. Paton, J. Hellstrom, B. Paul, J. Woodhead, J. Hergt, Iolite: Freeware for the visualisation and processing of mass spectrometric data. *Journal of Analytical Atomic Spectrometry* **26**, 2508-2518 (2011).
2. J. D. Woodhead, J. Hellstrom, J. M. Hergt, A. Greig, R. Maas, Isotopic and elemental imaging of geological materials by laser ablation inductively coupled plasma-mass spectrometry. *Geostandards and Geoanalytical Research* **31**, 331-343 (2007).
3. B. S. Kamber, A. Greig, K. D. Collerson, A new estimate for the composition of weathered young upper continental crust from alluvial sediments, Queensland, Australia. *Geochimica et Cosmochimica Acta* **69**, 1041-1058 (2005).
4. D. Asael *et al.*, Coupled molybdenum, iron and uranium stable isotopes as oceanic paleoredox proxies during the Paleoproterozoic Shunga Event. *Chemical Geology* **362**, 193-210 (2013).
5. V. Busigny *et al.*, Iron isotopes in an Archean ocean analogue. *Geochimica et Cosmochimica Acta* **133**, 443-462 (2014).
6. M.-A. Millet, J. A. Baker, C. E. Payne, Ultra-precise stable Fe isotope measurements by high resolution multiple-collector inductively coupled plasma mass spectrometry with a 57Fe–58Fe double spike. *Chemical Geology* **304**, 18-25 (2012).
7. K. Dideriksen, J. Baker, S. Stipp, Iron isotopes in natural carbonate minerals determined by MC-ICP-MS with a 58Fe–54Fe double spike. *Geochimica et Cosmochimica Acta* **70**, 118-132 (2006).
8. D.-H. Du *et al.*, Origin of heavy Fe isotope compositions in high-silica igneous rocks: A rhyolite perspective. *Geochimica et Cosmochimica Acta* **218**, 58-72 (2017).
9. H. Ye *et al.*, Updating the Geologic Barcodes for South China: Discovery of Late Archean Banded Iron Formations in the Yangtze Craton. *Scientific reports* **7**, 15082 (2017).
10. A. Heimann, B. L. Beard, C. M. Johnson, The role of volatile exsolution and sub-solidus fluid/rock interactions in producing high 56Fe/54Fe ratios in siliceous igneous rocks. *Geochimica et Cosmochimica Acta* **72**, 4379-4396 (2008).
11. P. R. Craddock, N. Dauphas, Iron isotopic compositions of geological reference materials and chondrites. *Geostandards and Geoanalytical Research* **35**, 101-123 (2011).
12. T. Gevers, An ancient tillite in South West Africa. *Trans. Geol. Soc. S. Afr* **34**, 1-17 (1931).
13. K. Hoffmann, A. Prave, A preliminary note on a revised subdivision and regional correlation of the Otavi Group based on glaciogenic diamictites and associated cap dolostones. *Communications of the Geological Survey of Namibia* **11**, 77-82 (1996).
14. P. F. Hoffman *et al.*, Sedimentary depocenters on Snowball Earth: Case studies from the Sturtian Chuos Formation in northern Namibia. *Geosphere* **13**, 811-837 (2017).
15. A. D. Rooney *et al.*, Re-Os geochronology and coupled Os-Sr isotope constraints on the Sturtian snowball Earth. *Proceedings of the National Academy of Sciences* **111**, 51-56 (2014).
16. A. D. Rooney, J. V. Strauss, A. D. Brandon, F. A. Macdonald, A Cryogenian chronology: Two long-lasting synchronous Neoproterozoic glaciations. *Geology* **43**, 459-462 (2015).
17. P. Hoffman, D. Hawkins, C. Isachsen, S. Bowring, Precise U-Pb zircon ages for early Damaran magmatism in the Summas Mountains and Welwitschia Inlier, northern Damara belt, Namibia. *Communications of the geological survey of Namibia* **11**, 47-52 (1996).
18. R. M. Miller, The Geology of Namibia. Volume 2: Neoproterozoic to Lower Palaeozoic. *Ministry of Mines and Energy, Windhoek, Namibia* (2008).
19. M. W. Wallace, A. vS Hood, E. M. Woon, K.-H. Hoffmann, C. P. Reed, Enigmatic chambered structures in Cryogenian reefs: The oldest sponge-grade organisms? *Precambrian Research* **255**, 109-123 (2014).
20. R. M. Miller, "The Pan-African Damara Orogen of South West Africa/Namibia" in Evolution of the Damara Orogen of South West Africa/Namibia. (1983).
21. P. Hoffman, G. Halverson, Otavi Group of the Western Northern Platform, the Eastern Kaoko Zone and the Western Northern Margin Zone. (2008).

22. M. A. Lechte, M. W. Wallace, K.-H. Hoffmann, Glacio-marine iron formation deposition in a c. 700 Ma glaciated margin: insights from the Chuos Formation, Namibia. *Geological Society, London, Special Publications* **475** (2018).
23. F. R. de Souza, H. A. Nalini jr, A. T. de Abreu, In-situ LA-ICP-MS and EMP trace element analyses of hematite: Insight into the geochemical signature of the Neoproterozoic Urucum iron formation, Brazil. *Journal of South American Earth Sciences*, 102313 (2019).
24. W. V. Preiss *et al.*, The glacial succession of Sturtian age in South Australia: the Yudnamutana Subgroup. *Geological Society, London, Memoirs* **36**, 701-712 (2011).
25. C. Dalgarno, J. Johnson, The Holowilena ironstone, a Sturtian glacigene unit. *Quart, geol. Notes, geol. Surv. S. Aust* **13** (1965).
26. G. M. Cox *et al.*, South Australian U-Pb zircon (CA-ID-TIMS) age supports globally synchronous Sturtian deglaciation. *Precambrian Research* **315**, 257-263 (2018).
27. W. Preiss, The Adelaide Geosyncline of South Australia and its significance in Neoproterozoic continental reconstruction. *Precambrian Research* **100**, 21-63 (2000).
28. W. V. Preiss, *The Adelaide Geosyncline: Late Proterozoic stratigraphy, sedimentation, palaeontology and tectonics* (Department of Mines and Energy, 1987).
29. M. A. Lechte, M. W. Wallace, Sedimentary and tectonic history of the Holowilena Ironstone, a Neoproterozoic iron formation in South Australia. *Sedimentary Geology* **329**, 211-224 (2015).
30. D. P. Le Heron, G. Cox, A. Trundley, A. S. Collins, Two Cryogenian glacial successions compared: Aspects of the Sturt and Elatina sediment records of South Australia. *Precambrian Research* **186**, 147-168 (2011).
31. J. A. Giddings, M. W. Wallace, Sedimentology and C-isotope geochemistry of the 'Sturtian'cap carbonate, South Australia. *Sedimentary Geology* **216**, 1-14 (2009).
32. R. Coats, W. Preiss, Stratigraphy of the Umberatana Group. *Preiss WV compiler. The Adelaide Geosyncline: Late Proterozoic stratigraphy, sedimentation, palaeontology and tectonics*, 125-209 (1987).
33. J. Foden, M. A. Elburg, J. Dougherty-Page, A. Burtt, The timing and duration of the Delamerian Orogeny: correlation with the Ross Orogen and implications for Gondwana assembly. *The Journal of Geology* **114**, 189-210 (2006).
34. N. J. Beukes, J. Gutzmer, Origin and paleoenvironmental significance of major iron formations at the Archean-Paleoproterozoic boundary. *Reviews in Economic Geology* **15**, 5-47 (2008).
35. B. Lottermoser, P. Ashley, Geochemistry, petrology and origin of Neoproterozoic ironstones in the eastern part of the Adelaide geosyncline, South Australia. *Precambrian Research* **101**, 49-67 (2000).
36. D. Hewett, New formation names to be used in the Kingston Range, Ivanpah Quadrangle, California. *Journal of the Washington Academy of Sciences* **30**, 239-240 (1940).
37. A. Prave, Two diamictites, two cap carbonates, two δ13C excursions, two rifts: the Neoproterozoic Kingston Peak Formation, Death Valley, California. *Geology* **27**, 339-342 (1999).
38. F. A. Macdonald *et al.*, The Laurentian record of Neoproterozoic glaciation, tectonism, and eukaryotic evolution in Death Valley, California. *Geological Society of America Bulletin* **125**, 1203-1223 (2013).
39. B. Burchfiel, D. S. Cowan, G. A. Davis, "Tectonic overview of the Cordilleran orogen in the western United States" in The Cordilleran orogen: conterminous US, B. C. Burchfiel, P. W. Lipman, M. L. Zoback, Eds. (Geological Society of America, Boulder, Colorado, USA, 1992).
40. L. Wright, B. Troxel, E. Williams, M. Roberts, P. Diehl, Precambrian sedimentary environments of the Death Valley region, eastern California. *Geologic features of Death Valley, California: California Division of Mines and Geology Special Report* **106**, 7-15 (1976).
41. M. A. Lechte, M. W. Wallace, A. van Smeerdijk Hood, N. Planavsky, Cryogenian iron formations in the glaciogenic Kingston Peak Formation, California. *Precambrian Research* **310**, 443-462 (2018).
42. C. Eyles, N. Eyles, Glacial deposits. *Facies Models* **4**, 73-104 (2010).

43. C. Eyles, N. Eyles, A. Miall, Models of glaciomarine sedimentation and their application to the interpretation of ancient glacial sequences. *Palaeogeography, Palaeoclimatology, Palaeoecology* **51**, 15-84 (1985).
44. M. Edwards, Glacial environments. *Sedimentary environments and facies*, 445-470 (1986).
45. E. Arnaud, J. L. Etienne, Recognition of glacial influence in Neoproterozoic sedimentary successions. *Geological Society, London, Memoirs* **36**, 39-50 (2011).
46. G. S. Boulton, M. Deynoux, Sedimentation in glacial environments and the identification of tills and tillites in ancient sedimentary sequences. *Precambrian Research* **15**, 397-422 (1981).
47. M. J. Hambrey, N. F. Glasser, Discriminating glacier thermal and dynamic regimes in the sedimentary record. *Sedimentary Geology* **251**, 1-33 (2012).
48. T. Naish *et al.*, Obliquity-paced Pliocene West Antarctic ice sheet oscillations. *Nature* **458**, 322 (2009).
49. K. Brodzikowski, A. Van Loon, A systematic classification of glacial and periglacial environments, facies and deposits. *Earth-Science Reviews* **24**, 297-381 (1987).
50. A. Elverhøi, S. L. Pfirman, A. Solheim, B. B. Larssen, Glaciomarine sedimentation in epicontinental seas exemplified by the northern Barents Sea. *Marine Geology* **85**, 225-250 (1989).
51. R. D. Powell, A. Elverhøi (1989) Modern glacimarine environments: Glacial and marine controls of modern lithofacies and biofacies. in *Marine Geology* (Elsevier, Amsterdam, Netherlands), p 416.
52. D. Evans, E. Phillips, J. Hiemstra, C. Auton, Subglacial till: formation, sedimentary characteristics and classification. *Earth-Science Reviews* **78**, 115-176 (2006).
53. G. Boulton (1982) Subglacial processes and the development of glacial bedforms. in *Research in Glacial, Glacio-Fluvial and Glacio-Lacustrine Systems. Proceedings of the 6 th Guelph Symposium on Geomorphology, 1980. 1982. p 1-31, 13 fig, 33 ref.*
54. M. E. Busfield, D. P. Le Heron, Glacitectonic deformation in the Chuos Formation of northern Namibia: implications for Neoproterozoic ice dynamics. *Proceedings of the Geologists' Association* **124**, 778-789 (2013).
55. G. S. Boulton, Modern Arctic glaciers as depositional models for former ice sheets. *Journal of the Geological Society* **128**, 361-393 (1972).
56. C. L. Batchelor, J. A. Dowdeswell, Ice-sheet grounding-zone wedges (GZWs) on high-latitude continental margins. *Marine Geology* **363**, 65-92 (2015).
57. R. D. Powell, Glacimarine processes at grounding-line fans and their growth to ice-contact deltas. *Geological Society, London, Special Publications* **53**, 53-73 (1990).
58. D. A. Stow, Laurentian Fan: morphology, sediments, processes, and growth pattern. *AAPG bulletin* **65**, 375-393 (1981).
59. D. Le Heron, The significance of ice-rafted debris in Sturtian glacial successions. *Sedimentary Geology* **322**, 19-33 (2015).
60. S. Carter, H. Fricker, The supply of subglacial meltwater to the grounding line of the Siple Coast, West Antarctica. *Annals of Glaciology* **53**, 267-280 (2012).
61. H. M. Dierssen, R. C. Smith, M. Vernet, Glacial meltwater dynamics in coastal waters west of the Antarctic peninsula. *Proceedings of the National Academy of Sciences* **99**, 1790-1795 (2002).
62. N. Eyles, The role of meltwater in glacial processes. *Sedimentary Geology* **190**, 257-268 (2006).
63. G. M. Ashley, "Rhythmic sedimentation in glacial lake Hitchcock, Massachusetts-Connecticut", . Ed. (Society of Economic Paleontologists and Mineralogists Special Publication, 1975), vol. 23, pp. 304-320.
64. G. Brown, M. Tranter, M. Sharp, T. Davies, S. Tsiouris, Dissolved oxygen variations in Alpine glacial meltwaters. *Earth Surface Processes and Landforms* **19**, 247-253 (1994).
65. R. Souchez, L. Janssens, M. Lemmens, B. Stauffer, Very low oxygen concentration in basal ice from Summit, Central Greenland. *Geophysical research letters* **22**, 2001-2004 (1995).

66. M. Tranter, M. Skidmore, J. Wadham, Hydrological controls on microbial communities in subglacial environments. *Hydrological Processes: An International Journal* **19**, 995-998 (2005).
67. A. Jenkins, The impact of melting ice on ocean waters. *Journal of Physical Oceanography* **29**, 2370-2381 (1999).
68. J. Wadham, M. Tranter, S. Tulaczyk, M. Sharp, Subglacial methanogenesis: a potential climatic amplifier? *Global Biogeochemical Cycles* **22** (2008).
69. M. Tranter, G. Brown, R. Raiswell, M. Sharp, A. Gurnell, A conceptual model of solute acquisition by Alpine glacial meltwaters. *Journal of Glaciology* **39**, 573-581 (1993).
70. J. A. Mikucki *et al.*, A Contemporary Microbially Maintained Subglacial Ferrous" Ocean". *Science* **324**, 397-400 (2009).
71. J. Wadham, R. Cooper, M. Tranter, S. Bottrell, Evidence for widespread anoxia in the proglacial zone of an Arctic glacier. *Chemical geology* **243**, 1-15 (2007).
72. T. D. Irvine-Fynn, A. J. Hodson, B. J. Moorman, G. Vatne, A. L. Hubbard, Polythermal glacier hydrology: A review. *Reviews of Geophysics* **49** (2011).
73. M. L. Skidmore, M. J. Sharp, Drainage system behaviour of a High-Arctic polythermal glacier. *Annals of Glaciology* **28**, 209-215 (1999).
74. E. Rignot, S. S. Jacobs, Rapid bottom melting widespread near Antarctic ice sheet grounding lines. *Science* **296**, 2020-2023 (2002).
75. H. A. Fricker, T. Scambos, R. Bindschadler, L. Padman, An active subglacial water system in West Antarctica mapped from space. *Science* **315**, 1544-1548 (2007).
76. E. Lewis, R. Perkin, Ice pumps and their rates. *Journal of Geophysical Research: Oceans* **91**, 11756-11762 (1986).
77. A. Jenkins, Convection-driven melting near the grounding lines of ice shelves and tidewater glaciers. *Journal of Physical Oceanography* **41**, 2279-2294 (2011).
78. R. L. Hooke, *Principles of glacier mechanics* (Cambridge university press, 2005).
79. I. J. Hewitt, Modelling distributed and channelized subglacial drainage: the spacing of channels. *Journal of Glaciology* **57**, 302-314 (2011).
80. A. L. Lowe, J. B. Anderson, Evidence for abundant subglacial meltwater beneath the paleo-ice sheet in Pine Island Bay, Antarctica. *Journal of Glaciology* **49**, 125-138 (2003).
81. J. A. Piotrowski, Subglacial hydrology in north-western Germany during the last glaciation: groundwater flow, tunnel valleys and hydrological cycles. *Quaternary Science Reviews* **16**, 169-185 (1997).
82. M. Tranter *et al.*, Variability in the chemical composition of in situ subglacial meltwaters. *Hydrological Processes* **11**, 59-77 (1997).
83. W. S. B. Paterson, *The physics of glaciers* (Elsevier, 2016).
84. J.-O. Andreasen, Seasonal surface-velocity variations on a sub-polar glacier in West Greenland. *Journal of Glaciology* **31**, 319-323 (1985).
85. F. Pattyn, Antarctic subglacial conditions inferred from a hybrid ice sheet/ice stream model. *Earth and Planetary Science Letters* **295**, 451-461 (2010).
86. G. Boulton, The role of thermal regime in glacial sedimentation. *Polar geomorphology* **4**, 1-19 (1972).
87. J. Evans, C. Pudsey, Sedimentation associated with Antarctic Peninsula ice shelves: implications for palaeoenvironmental reconstructions of glacimarine sediments. *Journal of the Geological Society* **159**, 233-237 (2002).
88. E. W. Domack, P. T. Harris, A new depositional model for ice shelves, based upon sediment cores from the Ross Sea and the Mac. Robertson shelf, Antarctica. *Annals of Glaciology* **27**, 281-284 (1998).
89. C. J. Pudsey, J. Evans, First survey of Antarctic sub–ice shelf sediments reveals mid-Holocene ice shelf retreat. *Geology* **29**, 787-790 (2001).

90. E. W. Domack, E. A. Jacobson, S. Shipp, J. B. Anderson, Late Pleistocene–Holocene retreat of the West Antarctic Ice-Sheet system in the Ross Sea: Part 2—sedimentologic and stratigraphic signature. *Geological Society of America Bulletin* **111**, 1517-1536 (1999).
91. D. Le Heron, S. Tofaif, T. Vandyk, D. Ali, A diamictite dichotomy: Glacial conveyor belts and olistostromes in the Neoproterozoic of Death Valley, California, USA. *Geology* **45**, 31-34 (2017).
92. N. Eyles, N. Januszczak, 'Zipper-rift': a tectonic model for Neoproterozoic glaciations during the breakup of Rodinia after 750 Ma. *Earth-Science Reviews* **65**, 1-73 (2004).
93. D. Nascimento, A. Ribeiro, R. Trouw, R. Schmitt, C. Passchier, Stratigraphy of the Neoproterozoic Damara Sequence in northwest Namibia: Slope to basin sub-marine mass-transport deposits and olistolith fields. *Precambrian Research* **278**, 108-125 (2016).
94. D. P. Le Heron, M. E. Busfield, F. Kamona, An interglacial on snowball Earth? Dynamic ice behaviour revealed in the Chuos Formation, Namibia. *Sedimentology* **60**, 411-427 (2013).
95. D. P. Le Heron, G. Cox, A. Trundley, A. Collins, Sea ice− free conditions during the Sturtian glaciation (early Cryogenian), South Australia. *Geology* **39**, 31-34 (2011).
96. M. Busfield, D. Le Heron, Sequencing the Sturtian icehouse: dynamic ice behaviour in South Australia. *Journal of the Geological Society* **171**, 443-456 (2014).
97. J. M. Miller, Glacial and syntectonic sedimentation: The upper Proterozoic Kingston Peak Formation, southern Panamint Range, eastern California. *Geological Society of America Bulletin* **96**, 1537-1553 (1985).
98. D. P. Le Heron, M. E. Busfield, A. R. Prave, Neoproterozoic ice sheets and olistoliths: multiple glacial cycles in the Kingston Peak Formation, California. *Journal of the Geological Society* **171**, 525-538 (2014).
99. M. E. Busfield, D. P. Le Heron, A Neoproterozoic ice advance sequence, Sperry Wash, California. *Sedimentology* **63**, 307-330 (2016).
100. G. Yeo, The late Proterozoic Rapitan glaciation in the northern Cordillera. *Proterozoic Basins of Canada* **81** (1981).
101. I. Lønne, W. Nemec, L. Blikra, T. Lauritsen, Sedimentary architecture and dynamic stratigraphy of a marine ice-contact system. *Journal of Sedimentary Research* **71**, 922-943 (2001).
102. D. P. Le Heron, M. E. Busfield, D. O. Ali, S. Al Tofaif, T. M. Vandyk, The Cryogenian record in the southern Kingston Range, California: The thickest Death Valley succession in the hunt for a GSSP. *Precambrian Research* (2017).
103. G. Henry, I. Stanistreet, K. Maiden, Preliminary results of a sedimentological study of the Chuos Formation in the Central Zone of the Damara Orogen: evidence for mass flow processes and glacial activity. *Communications of the Geological Survey of Namibia* **2**, 75-92 (1986).
104. M. Lechte, M. Wallace, Sub–ice shelf ironstone deposition during the Neoproterozoic Sturtian glaciation. *Geology* **44**, 891-894 (2016).
105. W. Harland, Evidence of Late Precambrian glaciation and its significance. *Problems in Palaeoclimatology* **705**, 119-149 (1964).
106. D. A. Evans, Stratigraphic, geochronological, and paleomagnetic constraints upon the Neoproterozoic climatic paradox. *American Journal of Science* **300**, 347-433 (2000).
107. D. Mawson (1949) The late Precambrian ice-age and glacial record of the Bibliando dome. in *J. Proc. Roy. Soc. New South Wales*, pp 150-174.
108. D. I. Benn *et al.*, Orbitally forced ice sheet fluctuations during the Marinoan Snowball Earth glaciation. *Nature Geoscience* **8**, 704 (2015).
109. P. F. Hoffman *et al.*, Snowball Earth climate dynamics and Cryogenian geology-geobiology. *Science Advances* **3**, e1600983 (2017).
110. C. McKay, Thickness of tropical ice and photosynthesis on a snowball Earth. *Geophysical research letters* **27**, 2153-2156 (2000).
111. A. S. Merdith *et al.*, A full-plate global reconstruction of the Neoproterozoic. *Gondwana Research* **50**, 84-134 (2017).

112. P. Hoffman, Vreeland Diamictites–Neoproterozoic glaciogenic slope deposits, Rocky Mountains, northeast British Columbia. *Bulletin of canadian petroleum geology* **48**, 360-363 (2000).
113. D. S. Abbot *et al.*, Robust elements of Snowball Earth atmospheric circulation and oases for life. *Journal of Geophysical Research: Atmospheres* **118**, 6017-6027 (2013).
114. Y. Ashkenazy, E. Tziperman, Variability, instabilities, and eddies in a Snowball Ocean. *Journal of Climate* **29**, 869-888 (2016).
115. J. Liu, R. Powell, Relation of ice face melting structures to oceanic characters using remotely operated vehicle observations, Mackay Glacier Tongue, Granite Harbor. *Antarctic Journal of the United States* **31**, 72-74 (1996).
116. A. M. Spencer (1971) Late pre-Cambrian glaciation in Scotland. (Geological Society of London).
117. J. Leather, P. A. Allen, M. D. Brasier, A. Cozzi, Neoproterozoic snowball Earth under scrutiny: Evidence from the Fiq glaciation of Oman. *Geology* **30**, 891-894 (2002).
118. D. Condon, A. Prave, D. Benn, Neoproterozoic glacial-rainout intervals: observations and implications. *Geology* **30**, 35-38 (2002).
119. D. P. Le Heron, M. E. Busfield, Pulsed iceberg delivery driven by Sturtian ice sheet dynamics: An example from Death Valley, California. *Sedimentology* **63**, 331-349 (2016).
120. P. A. Allen, J. L. Etienne, Sedimentary challenge to snowball Earth. *Nature Geoscience* **1**, 817 (2008).
121. J. Etienne, P. Allen, R. Rieu, E. Le Guerroué, M. Hambrey, Neoproterozoic glaciated basins: a critical review of the Snowball Earth hypothesis by comparison with Phanerozoic glaciations. *SPECIAL PUBLICATION-INTERNATIONAL ASSOCIATION OF SEDIMENTOLOGISTS* **39**, 343 (2007).
122. T. Vandyk *et al.*, Temperate glaciation on a Snowball Earth: Glaciological and palaeogeographic insights from the Cryogenian Yuermeinak Formation of NW China. *Precambrian Research*, 105362 (2019).
123. C. Klein, N. J. Beukes, Sedimentology and geochemistry of the glaciogenic late Proterozoic Rapitan iron-formation in Canada. *Economic Geology* **88**, 542-565 (1993).
124. C. H. Eyles, N. Eyles, Glaciomarine model for upper Precambrian diamictites of the Port Askaig Formation, Scotland. *Geology* **11**, 692-696 (1983).
125. I. Fairchild, M. J. Hambrey, B. Spiro, T. Jefferson, Late Proterozoic glacial carbonates in northeast Spitsbergen: new insights into the carbonate–tillite association. *Geological Magazine* **126**, 469-490 (1989).
126. D. J. Wingham, M. J. Siegert, A. Shepherd, A. S. Muir, Rapid discharge connects Antarctic subglacial lakes. *Nature* **440**, 1033 (2006).
127. A. M. Le Brocq *et al.*, Evidence from ice shelves for channelized meltwater flow beneath the Antarctic Ice Sheet. *Nature Geoscience* **6**, 945 (2013).
128. T. W. Lyons, S. Severmann, A critical look at iron paleoredox proxies: New insights from modern euxinic marine basins. *Geochimica et Cosmochimica Acta* **70**, 5698-5722 (2006).
129. R. Guilbaud, S. W. Poulton, N. J. Butterfield, M. Zhu, G. A. Shields-Zhou, A global transition to ferruginous conditions in the early Neoproterozoic oceans. *Nature Geoscience* **8**, 466 (2015).
130. D. Thomson, R. H. Rainbird, N. Planavsky, T. W. Lyons, A. Bekker, Chemostratigraphy of the Shaler Supergroup, Victoria Island, NW Canada: A record of ocean composition prior to the Cryogenian glaciations. *Precambrian Research* **263**, 232-245 (2015).
131. B. W. Johnson, S. W. Poulton, C. Goldblatt, Marine oxygen production and open water supported an active nitrogen cycle during the Marinoan Snowball Earth. *Nature Communications* **8**, 1316 (2017).
132. S. W. Poulton, D. E. Canfield, Ferruginous conditions: a dominant feature of the ocean through Earth's history. *Elements* **7**, 107-112 (2011).
133. E. Percak-Dennett *et al.*, Iron isotope fractionation during microbial dissimilatory iron oxide reduction in simulated Archaean seawater. *Geobiology* **9**, 205-220 (2011).

134. K. O. Konhauser *et al.*, Iron formations: A global record of Neoarchaean to Palaeoproterozoic environmental history. *Earth-Science Reviews* **172**, 140-177 (2017).
135. R. E. Kopp, J. L. Kirschvink, I. A. Hilburn, C. Z. Nash, The Paleoproterozoic snowball Earth: a climate disaster triggered by the evolution of oxygenic photosynthesis. *Proceedings of the National Academy of Sciences of the United States of America* **102**, 11131-11136 (2005).
136. J. L. Kirschvink *et al.*, Paleoproterozoic snowball Earth: Extreme climatic and geochemical global change and its biological consequences. *Proceedings of the National Academy of Sciences* **97**, 1400-1405 (2000).
137. T. Hamade, K. O. Konhauser, R. Raiswell, S. Goldsmith, R. C. Morris, Using Ge/Si ratios to decouple iron and silica fluxes in Precambrian banded iron formations. *Geology* **31**, 35-38 (2003).
138. B. Bühn, I. G. Stanistreet, M. Okrusch, Late Proterozoic outer shelf manganese and iron deposits at Otjosondu (Namibia) related to the Damaran oceanic opening. *Economic Geology* **87**, 1393-1411 (1992).
139. H. Urban, B. Stribrny, H. Lippolt, Iron and manganese deposits of the Urucum district, Mato Grosso do Sul, Brazil. *Economic Geology* **87**, 1375-1392 (1992).
140. R. Byrne, E. Sholkovitz, Marine chemistry and geochemistry of the lanthanides. *Handbook on the physics and chemistry of rare earths* **23**, 497-593 (1996).
141. C. R. German, H. Elderfield, Application of the Ce anomaly as a paleoredox indicator: the ground rules. *Paleoceanography* **5**, 823-833 (1990).
142. B. Fryer, Rare earth evidence in iron-formations for changing Precambrian oxidation states. *Geochimica et Cosmochimica Acta* **41**, 361-367 (1977).
143. M. Bau, P. Dulski, Distribution of yttrium and rare-earth elements in the Penge and Kuruman iron-formations, Transvaal Supergroup, South Africa. *Precambrian Research* **79**, 37-55 (1996).
144. M. G. Lawrence, B. S. Kamber, The behaviour of the rare earth elements during estuarine mixing—revisited. *Marine Chemistry* **100**, 147-161 (2006).
145. M. Bau, A. Koschinsky, Oxidative scavenging of cerium on hydrous Fe oxide: evidence from the distribution of rare earth elements and yttrium between Fe oxides and Mn oxides in hydrogenetic ferromanganese crusts. *Geochemical Journal* **43**, 37-47 (2009).
146. M. Bau, Scavenging of dissolved yttrium and rare earths by precipitating iron oxyhydroxide: experimental evidence for Ce oxidation, Y-Ho fractionation, and lanthanide tetrad effect. *Geochimica et Cosmochimica Acta* **63**, 67-77 (1999).
147. J. W. Moffett, Microbially mediated cerium oxidation in sea water. *Nature* **345**, 421 (1990).
148. T. Kuhn, M. Bau, N. Blum, P. Halbach, Origin of negative Ce anomalies in mixed hydrothermal–hydrogenetic Fe–Mn crusts from the Central Indian Ridge. *Earth and Planetary Science Letters* **163**, 207-220 (1998).
149. A. Ohta, I. Kawabe, REE (III) adsorption onto Mn dioxide (δ-MnO2) and Fe oxyhydroxide: Ce (III) oxidation by δ-MnO2. *Geochimica et Cosmochimica Acta* **65**, 695-703 (2001).
150. J. Slack, T. Grenne, A. Bekker, O. Rouxel, P. Lindberg, Suboxic deep seawater in the late Paleoproterozoic: evidence from hematitic chert and iron formation related to seafloor-hydrothermal sulfide deposits, central Arizona, USA. *Earth and Planetary Science Letters* **255**, 243-256 (2007).
151. M. Bau *et al.*, Discriminating between different genetic types of marine ferro-manganese crusts and nodules based on rare earth elements and yttrium. *Chemical Geology* **381**, 1-9 (2014).
152. L. S. Prakash *et al.*, Distribution of REEs and yttrium among major geochemical phases of marine Fe–Mn-oxides: Comparative study between hydrogenous and hydrothermal deposits. *Chemical Geology* **312**, 127-137 (2012).
153. H. Elderfield, The oceanic chemistry of the rare-earth elements. *Philosophical Transactions of the Royal Society of London. Series A, Mathematical and Physical Sciences* **325**, 105-126 (1988).
154. H. Elderfield, C. Hawkesworth, M. J. Greaves, S. Calvert, Rare-earth element geochemistry of oceanic ferromanganese nodules and associated sediments. *Geochimica et Cosmochimica Acta* **45**, 15 (1981).

155. R. M. Sherrell, M. P. Field, G. Ravizza, Uptake and fractionation of rare earth elements on hydrothermal plume particles at 9 45′ N, East Pacific Rise. *Geochimica et Cosmochimica Acta* **63**, 1709-1722 (1999).
156. C. German, G. Klinkhammer, J. Edmond, A. Mura, H. Elderfield, Hydrothermal scavenging of rare-earth elements in the ocean. *Nature* **345**, 516 (1990).
157. E. D. Goldberg, M. Koide, R. Schmitt, R. H. Smith, Rare-Earth distributions in the marine environment. *Journal of Geophysical Research* **68**, 4209-4217 (1963).
158. E. H. De Carlo, X.-Y. Wen, M. Irving, The influence of redox reactions on the uptake of dissolved Ce by suspended Fe and Mn oxide particles. *Aquatic Geochemistry* **3**, 357-389 (1997).
159. J. Schijf, E. A. Christenson, R. H. Byrne, YREE scavenging in seawater: A new look at an old model. *Marine Chemistry* **177**, 460-471 (2015).
160. N. Planavsky *et al.*, Rare earth element and yttrium compositions of Archean and Paleoproterozoic Fe formations revisited: new perspectives on the significance and mechanisms of deposition. *Geochimica et Cosmochimica Acta* **74**, 6387-6405 (2010).
161. T. Angerer, S. G. Hagemann, D. Walde, G. P. Halverson, A. J. Boyce, Multiple metal sources in the glaciomarine facies of the Neoproterozoic Jacadigo iron formation in the "Santa Cruz deposit", Corumbá, Brazil. *Precambrian Research* (2016).
162. Y. Kato, K. E. Yamaguchi, H. Ohmoto, Rare earth elements in Precambrian banded iron formations: Secular changes ofCe andEu anomalies and evolution of atmospheric oxygen. *Evolution of Early Earth's Atmosphere, Hydrosphere, and Biosphere: Constraints from Ore Deposits* **198**, 269 (2006).
163. A. E. Isley, D. H. Abbott, Plume-related mafic volcanism and the deposition of banded iron formation. *Journal of Geophysical Research: Solid Earth* **104**, 15461-15477 (1999).
164. M. W. Wallace *et al.*, Oxygenation history of the Neoproterozoic to early Phanerozoic and the rise of land plants. *Earth and Planetary Science Letters* **466**, 12-19 (2017).
165. R. Tostevin *et al.*, Effective use of cerium anomalies as a redox proxy in carbonate-dominated marine settings. *Chemical Geology* **438**, 146-162 (2016).
166. R. Bolhar, A. Hofmann, M. Siahi, Y.-x. Feng, C. Delvigne, A trace element and Pb isotopic investigation into the provenance and deposition of stromatolitic carbonates, ironstones and associated shales of the∼ 3.0 Ga Pongola Supergroup, Kaapvaal Craton. *Geochimica et Cosmochimica Acta* **158**, 57-78 (2015).
167. B. S. Kamber, G. E. Webb, M. Gallagher, The rare earth element signal in Archaean microbial carbonate: information on ocean redox and biogenicity. *Journal of the Geological Society* **171**, 745-763 (2014).
168. A. C. Allwood, B. S. Kamber, M. R. Walter, I. W. Burch, I. Kanik, Trace elements record depositional history of an Early Archean stromatolitic carbonate platform. *Chemical Geology* **270**, 148-163 (2010).
169. H. J. de Baar, C. R. German, H. Elderfield, P. Van Gaans, Rare earth element distributions in anoxic waters of the Cariaco Trench. *Geochimica et Cosmochimica Acta* **52**, 1203-1219 (1988).
170. A. J. B. Smith, "The Iron Formations of Southern Africa" in Geology of Southwest Gondwana, S. Siegesmund, M. A. S. Basei, P. Oyhantçabal, S. Oriolo, Eds. (Springer International Publishing, Cham, 2018), pp. 469-491.
171. G. P. Halverson *et al.*, Fe isotope and trace element geochemistry of the Neoproterozoic syn-glacial Rapitan iron formation. *Earth and Planetary Science Letters* **309**, 100-112 (2011).
172. L.-J. Feng, J. Huang, D. Lu, Q.-R. Zhang, Major and trace element geochemistry of the Neoproterozoic syn-glacial Fulu iron formation, South China. *Geological Magazine*, 1-10 (2017).
173. G. M. Cox *et al.*, Neoproterozoic iron formation: An evaluation of its temporal, environmental and tectonic significance. *Chemical Geology* **362**, 232-249 (2013).
174. A. Cabral, J. Moore, B. Mapani, M. Koubová, C.-D. Sattler, Geochemical and mineralogical constraints on the genesis of the Otjosondu ferromanganese deposit, Namibia: hydrothermal

exhalative versus hydrogenetic (including snowball-earth) origins. *South African Journal of Geology* **114**, 57-76 (2011).
175. J. B. Maynard, The chemistry of manganese ores through time: a signal of increasing diversity of earth-surface environments. *Economic Geology* **105**, 535-552 (2010).
176. B. Bühn, I. G. Stanistreet, Insight into the enigma of Neoproterozoic manganese and iron formations from the perspective of supercontinental break-up and glaciation. *Geological Society, London, Special Publications* **119**, 81-90 (1997).
177. S. Viehmann *et al.*, Geochemical characterisation of Neoproterozoic marine habitats: Evidence from trace elements and Nd isotopes in the Urucum iron and manganese formations, Brazil. *Precambrian Research* **282**, 74-96 (2016).
178. W. Yu *et al.*, Genesis of Cryogenian Datangpo manganese deposit: Hydrothermal influence and episodic post-glacial ventilation of Nanhua Basin, South China. *Palaeogeography, palaeoclimatology, palaeoecology* **459**, 321-337 (2016).
179. J. Xiao, J. He, H. Yang, C. Wu, Comparison between Datangpo-type manganese ores and modern marine ferromanganese oxyhydroxide precipitates based on rare earth elements. *Ore Geology Reviews* **89**, 290-308 (2017).
180. L. A. Derry, S. B. Jacobsen, The chemical evolution of Precambrian seawater: Evidence from REEs in banded iron formations. *Geochimica et Cosmochimica Acta* **54**, 2965-2977 (1990).
181. U. Raye, P. K. Pufahl, T. K. Kyser, E. Ricard, E. E. Hiatt, The role of sedimentology, oceanography, and alteration on the δ56Fe value of the Sokoman Iron Formation, Labrador Trough, Canada. *Geochimica et Cosmochimica Acta* **164**, 205-220 (2015).
182. B. L. Beard *et al.*, Application of Fe isotopes to tracing the geochemical and biological cycling of Fe. *Chemical Geology* **195**, 87-117 (2003).
183. C. M. Johnson, B. L. Beard, C. Klein, N. J. Beukes, E. E. Roden, Iron isotopes constrain biologic and abiologic processes in banded iron formation genesis. *Geochimica et Cosmochimica Acta* **72**, 151-169 (2008).
184. C. M. Johnson, B. L. Beard, E. E. Roden, The iron isotope fingerprints of redox and biogeochemical cycling in modern and ancient Earth. *Annu. Rev. Earth Planet. Sci.* **36**, 457-493 (2008).
185. A. D. Czaja *et al.*, Biological Fe oxidation controlled deposition of banded iron formation in the ca. 3770 Ma Isua Supracrustal Belt (West Greenland). *Earth and Planetary Science Letters* **363**, 192-203 (2013).
186. W. Li, B. L. Beard, C. M. Johnson, Biologically recycled continental iron is a major component in banded iron formations. *Proceedings of the National Academy of Sciences* **112**, 8193-8198 (2015).
187. C. M. Johnson *et al.*, Isotopic fractionation between Fe (III) and Fe (II) in aqueous solutions. *Earth and Planetary Science Letters* **195**, 141-153 (2002).
188. L. Wu, E. M. Percak-Dennett, B. L. Beard, E. E. Roden, C. M. Johnson, Stable iron isotope fractionation between aqueous Fe (II) and model Archean ocean Fe–Si coprecipitates and implications for iron isotope variations in the ancient rock record. *Geochimica et Cosmochimica Acta* **84**, 14-28 (2012).
189. T. D. Bullen, A. F. White, C. W. Childs, D. V. Vivit, M. S. Schulz, Demonstration of significant abiotic iron isotope fractionation in nature. *Geology* **29**, 699-702 (2001).
190. O. J. Rouxel, A. Bekker, K. J. Edwards, Iron isotope constraints on the Archean and Paleoproterozoic ocean redox state. *Science* **307**, 1088-1091 (2005).
191. W. Li *et al.*, An anoxic, Fe (II)-rich, U-poor ocean 3.46 billion years ago. *Geochimica et Cosmochimica Acta* **120**, 65-79 (2013).
192. R. Zhang *et al.*, Transport and reaction of iron and iron stable isotopes in glacial meltwaters on Svalbard near Kongsfjorden: From rivers to estuary to ocean. *Earth and Planetary Science Letters* **424**, 201-211 (2015).

193. A. D. Czaja, M. J. Van Kranendonk, B. L. Beard, C. M. Johnson, A multistage origin for Neoarchean layered hematite-magnetite iron formation from the Weld Range, Yilgarn Craton, Western Australia. *Chemical Geology* **488**, 125-137 (2018).
194. N. Planavsky *et al.*, Iron isotope composition of some Archean and Proterozoic iron formations. *Geochimica et Cosmochimica Acta* **80**, 158-169 (2012).
195. Y. Lin, D. Tang, X. Shi, X. Zhou, K. Huang, Shallow-marine ironstones formed by microaerophilic iron-oxidizing bacteria in terminal Paleoproterozoic. *Gondwana Research* **76**, 1-18 (2019).
196. L. R. Croal, C. M. Johnson, B. L. Beard, D. K. Newman, Iron isotope fractionation by Fe (II)-oxidizing photoautotrophic bacteria 1. *Geochimica et cosmochimica acta* **68**, 1227-1242 (2004).
197. A. Kappler, C. Johnson, H. Crosby, B. Beard, D. Newman, Evidence for equilibrium iron isotope fractionation by nitrate-reducing iron (II)-oxidizing bacteria. *Geochimica et cosmochimica acta* **74**, 2826-2842 (2010).
198. A. Kappler, C. Pasquero, K. O. Konhauser, D. K. Newman, Deposition of banded iron formations by anoxygenic phototrophic Fe (II)-oxidizing bacteria. *Geology* **33**, 865-868 (2005).
199. F. Widdel *et al.*, Ferrous iron oxidation by anoxygenic phototrophic bacteria. *Nature* **362**, 834 (1993).
200. K. O. Konhauser *et al.*, Could bacteria have formed the Precambrian banded iron formations? *Geology* **30**, 1079-1082 (2002).
201. C. Chan, D. Emerson, G. Luther III, The role of microaerophilic Fe-oxidizing micro-organisms in producing banded iron formations. *Geobiology* **14**, 509-528 (2016).
202. K. L. Straub, B. E. Buchholz-Cleven, Enumeration and detection of anaerobic ferrous iron-oxidizing, nitrate-reducing bacteria from diverse European sediments. *Appl. Environ. Microbiol.* **64**, 4846-4856 (1998).
203. N. Planavsky *et al.*, Iron-oxidizing microbial ecosystems thrived in late Paleoproterozoic redox-stratified oceans. *Earth and Planetary Science Letters* **286**, 230-242 (2009).
204. S. G. Warren, R. E. Brandt, T. C. Grenfell, C. P. McKay, Snowball Earth: Ice thickness on the tropical ocean. *Journal of Geophysical Research: Oceans* **107** (2002).
205. A. Ehrenreich, F. Widdel, Anaerobic oxidation of ferrous iron by purple bacteria, a new type of phototrophic metabolism. *Applied and environmental microbiology* **60**, 4517-4526 (1994).
206. S. Brake, S. Hasiotis, H. Dannelly, K. Connors, Eukaryotic stromatolite builders in acid mine drainage: Implications for Precambrian iron formations and oxygenation of the atmosphere? *Geology* **30**, 599-602 (2002).
207. D. Le Heron, M. Busfield, E. Le Ber, A. Kamona, Neoproterozoic ironstones in northern Namibia: Biogenic precipitation and Cryogenian glaciation. *Palaeogeography, Palaeoclimatology, Palaeoecology* **369**, 48-57 (2013).
208. E. Field *et al.*, Planktonic marine iron oxidizers drive iron mineralization under low-oxygen conditions. *Geobiology* **14**, 499-508 (2016).
209. B. L. Beard *et al.*, Iron isotope biosignatures. *Science* **285**, 1889-1892 (1999).
210. H. A. Crosby, C. M. Johnson, E. E. Roden, B. L. Beard, Coupled Fe (II)− Fe (III) electron and atom exchange as a mechanism for Fe isotope fractionation during dissimilatory iron oxide reduction. *Environmental science & technology* **39**, 6698-6704 (2005).
211. C. M. Johnson, B. L. Beard, N. J. Beukes, C. Klein, J. M. O'Leary, Ancient geochemical cycling in the Earth as inferred from Fe isotope studies of banded iron formations from the Transvaal Craton. *Contributions to Mineralogy and Petrology* **144**, 523-547 (2003).
212. S. Severmann, T. W. Lyons, A. Anbar, J. McManus, G. Gordon, Modern iron isotope perspective on the benthic iron shuttle and the redox evolution of ancient oceans. *Geology* **36**, 487-490 (2008).
213. H. Tsikos, A. Matthews, Y. Erel, J. M. Moore, Iron isotopes constrain biogeochemical redox cycling of iron and manganese in a Palaeoproterozoic stratified basin. *Earth and Planetary Science Letters* **298**, 125-134 (2010).

214. R. A. Wiesli, B. L. Beard, C. M. Johnson, Experimental determination of Fe isotope fractionation between aqueous Fe (II), siderite and "green rust" in abiotic systems. *Chemical Geology* **211**, 343-362 (2004).
215. A. Heimann *et al.*, Fe, C, and O isotope compositions of banded iron formation carbonates demonstrate a major role for dissimilatory iron reduction in~ 2.5 Ga marine environments. *Earth and Planetary Science Letters* **294**, 8-18 (2010).
216. E. A. Sperling *et al.*, Statistical analysis of iron geochemical data suggests limited late Proterozoic oxygenation. *Nature* **523**, 451 (2015).
217. W. B. Harland, M. J. Rudwick, The great infra-Cambrian ice age. *Scientific American* **211**, 28-37 (1964).
218. B. Runnegar, Palaeoclimate: loophole for snowball Earth. *Nature* **405**, 403 (2000).
219. J. L. Kirschvink, Late Proterozoic low-latitude global glaciation: the snowball Earth. (1992).
220. P. F. Hoffman, A. J. Kaufman, G. P. Halverson, D. P. Schrag, A Neoproterozoic snowball earth. *Science* **281**, 1342-1346 (1998).
221. J. Croll, *Climate and Time in their Geological Relations* (Daldy, Isbister & Co., London, 1875).
222. P. F. Hoffman, D. P. Schrag, The snowball Earth hypothesis: testing the limits of global change. *Terra Nova* **14**, 129-155 (2002).
223. R. A. Boyle, T. M. Lenton, H. T. Williams, Neoproterozoic 'snowball Earth'glaciations and the evolution of altruism. *Geobiology* **5**, 337-349 (2007).
224. J. J. Brocks *et al.*, The rise of algae in Cryogenian oceans and the emergence of animals. *Nature* **548**, 578 (2017).
225. W. Vincent *et al.*, Ice shelf microbial ecosystems in the high Arctic and implications for life on Snowball Earth. *Naturwissenschaften* **87**, 137-141 (2000).
226. M. Moczydłowska, The Ediacaran microbiota and the survival of Snowball Earth conditions. *Precambrian Research* **167**, 1-15 (2008).
227. D. P. Le Heron, The location and styles of ice-free "oases" during Neoproterozoic glaciations with evolutionary implications. *Geosciences* **2**, 90-108 (2012).
228. P. Hoffman, Cryoconite pans on Snowball Earth: supraglacial oases for Cryogenian eukaryotes? *Geobiology* **14**, 531-542 (2016).
229. S. M. Porter, The fossil record of early eukaryotic diversification. *The Paleontological Society Papers* **10**, 35-50 (2004).
230. N. J. Butterfield, Early evolution of the Eukaryota. *Palaeontology* **58**, 5-17 (2015).
231. E. Javaux, Early eukaryotes in Precambrian oceans. *Origins and evolution of life: An astrobiological perspective* **6**, 414 (2011).
232. A. H. Knoll, Paleobiological perspectives on early eukaryotic evolution. *Cold Spring Harbor Perspectives in Biology* **6**, a016121 (2014).
233. M. dos Reis *et al.*, Uncertainty in the timing of origin of animals and the limits of precision in molecular timescales. *Current Biology* **25**, 2939-2950 (2015).
234. D. H. Erwin *et al.*, The Cambrian conundrum: early divergence and later ecological success in the early history of animals. *science* **334**, 1091-1097 (2011).
235. C. Berney, J. Pawlowski, A molecular time-scale for eukaryote evolution recalibrated with the continuous microfossil record. *Proceedings of the Royal Society of London B: Biological Sciences* **273**, 1867-1872 (2006).
236. C. C. Loron *et al.*, Early fungi from the Proterozoic era in Arctic Canada. *Nature*, 1 (2019).
237. T. M. Gibson *et al.*, Precise age of Bangiomorpha pubescens dates the origin of eukaryotic photosynthesis. *Geology* (2017).
238. N. J. Butterfield, A. H. Knoll, K. Swett, A bangiophyte red alga from the Proterozoic of arctic Canada. *Science* **250**, 104-107 (1990).
239. N. J. Butterfield, A. H. Knoll, K. Swett, Paleobiology of the Neoproterozoic Svanbergfjellet Formation, Spitsbergen. *Lethaia* **27**, 76-76 (1994).

240. S. M. Porter, A. H. Knoll, Testate amoebae in the Neoproterozoic Era: evidence from vase-shaped microfossils in the Chuar Group, Grand Canyon. *Paleobiology* **26**, 360-385 (2000).
241. S. M. Porter, L. A. Riedman, Systematics of organic-walled microfossils from the ca. 780–740 Ma Chuar Group, Grand Canyon, Arizona. *Journal of Paleontology* **90**, 815-853 (2016).
242. D. J. Lahr *et al.*, Phylogenomics and morphological reconstruction of Arcellinida testate amoebae highlight diversity of microbial eukaryotes in the Neoproterozoic. *Current Biology* (2019).
243. S. M. Porter, R. Meisterfeld, A. H. Knoll, Vase-shaped microfossils from the Neoproterozoic Chuar Group, Grand Canyon: a classification guided by modern testate amoebae. *Journal of Paleontology* **77**, 409-429 (2003).
244. S. M. Porter, L. A. Riedman, Evolution: Ancient Fossilized Amoebae Find Their Home in the Tree. *Current Biology* **29**, R212-R215 (2019).
245. L. A. Riedman, S. M. Porter, C. R. Calver, Vase-shaped microfossil biostratigraphy with new data from Tasmania, Svalbard, Greenland, Sweden and the Yukon. *Precambrian Research* **319**, 19-36 (2018).
246. T. Bosak *et al.*, Possible early foraminiferans in post-Sturtian (716− 635 Ma) cap carbonates. *Geology* **40**, 67-70 (2012).
247. T. Bosak, F. Macdonald, D. Lahr, E. Matys, Putative cryogenian ciliates from Mongolia. *Geology* **39**, 1123-1126 (2011).
248. L. A. Dalton, T. Bosak, F. A. Macdonald, D. J. Lahr, S. B. Pruss, Preservational and morphological variability of assemblages of agglutinated eukaryotes in Cryogenian cap carbonates of northern Namibia. *Palaios* **28**, 67-79 (2013).
249. T. Bosak *et al.*, Agglutinated tests in post-Sturtian cap carbonates of Namibia and Mongolia. *Earth and Planetary Science Letters* **308**, 29-40 (2011).
250. P. A. Cohen, F. A. Macdonald, S. Pruss, E. Matys, T. Bosak, Fossils of putative marine algae from the Cryogenian glacial interlude of Mongolia. *Palaios* **30**, 238-247 (2015).
251. T. T. Isson *et al.*, Tracking the rise of eukaryotes to ecological dominance with zinc isotopes. *Geobiology* (2018).
252. S. Xiao, Q. Tang, After the boring billion and before the freezing millions: evolutionary patterns and innovations in the Tonian Period. *Emerging Topics in Life Sciences* **2**, 161-171 (2018).
253. H. J. Hofmann, The mid-Proterozoic Little Dal macrobiota, Mackenzie Mountains, north-west Canada. *Palaeontology* **28**, 331-354 (1985).
254. P. A. Cohen, J. V. Strauss, A. D. Rooney, M. Sharma, N. Tosca, Controlled hydroxyapatite biomineralization in an~ 810 million-year-old unicellular eukaryote. *Science Advances* **3**, e1700095 (2017).
255. K. Pang *et al.*, Nitrogen-fixing heterocystous cyanobacteria in the Tonian Period. *Current Biology* **28**, 616-622. e611 (2018).
256. S. M. Porter, Tiny vampires in ancient seas: evidence for predation via perforation in fossils from the 780–740 million-year-old Chuar Group, Grand Canyon, USA. *Proceedings of the Royal Society B: Biological Sciences* **283**, 20160221 (2016).
257. M. Dohrmann, G. Wörheide, Dating early animal evolution using phylogenomic data. *Scientific reports* **7**, 3599 (2017).
258. D. H. Erwin, Early metazoan life: divergence, environment and ecology. *Phil. Trans. R. Soc. B* **370**, 20150036 (2015).
259. R. C. Sprigg, Early Cambrian (?) jellyfishes from the Flinders Ranges, South Australia. *Transactions of the Royal Society of South Australia* **71**, 212-224 (1947).
260. D. A. Gold, B. Runnegar, J. G. Gehling, D. K. Jacobs, Ancestral state reconstruction of ontogeny supports a bilaterian affinity for Dickinsonia. *Evolution & Development* **17**, 315-324 (2015).
261. I. Bobrovskiy *et al.*, Ancient steroids establish the Ediacaran fossil Dickinsonia as one of the earliest animals. *Science* **361**, 1246-1249 (2018).
262. H. Hofmann, G. Narbonne, J. Aitken, Ediacaran remains from intertillite beds in northwestern Canada. *Geology* **18**, 1199-1202 (1990).

263. G. Burzynski (2017) Ediacaran Discs: Elucidating the Form and Function of the Discoid Fossils at the Root of Metazoan Evolution.
264. S. Xiao, M. Laflamme, On the eve of animal radiation: phylogeny, ecology and evolution of the Ediacara biota. *Trends in Ecology & Evolution* **24**, 31-40 (2009).
265. D. Grazhdankin, G. Gerdes, Ediacaran microbial colonies. *Lethaia* **40**, 201-210 (2007).
266. F. Neuweiler, E. C. Turner, D. J. Burdige, Early Neoproterozoic origin of the metazoan clade recorded in carbonate rock texture. *Geology* **37**, 475-478 (2009).
267. A. C. Maloof *et al.*, Possible animal-body fossils in pre-Marinoan limestones from South Australia. *Nature Geoscience* **3**, 653 (2010).
268. C. B. Brain *et al.*, The first animals: ca. 760-million-year-old sponge-like fossils from Namibia. *South African Journal of Science* **108**, 01-08 (2012).
269. J. B. Antcliffe, R. H. Callow, M. D. Brasier, Giving the early fossil record of sponges a squeeze. *Biological Reviews* **89**, 972-1004 (2014).
270. A. Muscente, F. M. Michel, J. G. Dale, S. Xiao, Assessing the veracity of Precambrian 'sponge'fossils using in situ nanoscale analytical techniques. *Precambrian Research* **263**, 142-156 (2015).
271. E. A. Sperling, R. G. Stockey, The temporal and environmental context of early animal evolution: considering all the ingredients of an 'explosion'. *Integrative and Comparative Biology* (2018).
272. G. D. Love *et al.*, Fossil steroids record the appearance of Demospongiae during the Cryogenian period. *Nature* **457**, 718 (2009).
273. J. A. Zumberge *et al.*, Demosponge steroid biomarker 26-methylstigmastane provides evidence for Neoproterozoic animals. *Nature ecology & evolution* **2**, 1709 (2018).
274. J. B. Antcliffe, Questioning the evidence of organic compounds called sponge biomarkers. *Palaeontology* **56**, 917-925 (2013).
275. B. J. Nettersheim *et al.*, Putative sponge biomarkers in unicellular Rhizaria question an early rise of animals. *Nature ecology & evolution*, 1 (2019).
276. J. Brocks *et al.*, Early sponges and toxic protists: possible sources of cryostane, an age diagnostic biomarker antedating Sturtian Snowball Earth. *Geobiology* **14**, 129-149 (2016).
277. J. P. Botting, L. A. Muir, Early sponge evolution: a review and phylogenetic framework. *Palaeoworld* **27**, 1-29 (2018).
278. A. H. Knoll, Proterozoic and Early Cambrian protists: evidence for accelerating evolutionary tempo. *Proceedings of the National Academy of Sciences* **91**, 6743-6750 (1994).
279. F. A. Corsetti, RESEARCH FOCUS: Life During Neoproterozoic Snowball Earth. *Geology* **43**, 559-560 (2015).
280. F. A. Corsetti, S. M. Awramik, D. Pierce, A complex microbiota from snowball Earth times: microfossils from the Neoproterozoic Kingston Peak Formation, Death Valley, USA. *Proceedings of the National Academy of Sciences* **100**, 4399-4404 (2003).
281. L. A. Riedman, S. M. Porter, G. P. Halverson, M. T. Hurtgen, C. K. Junium, Organic-walled microfossil assemblages from glacial and interglacial Neoproterozoic units of Australia and Svalbard. *Geology* **42**, 1011-1014 (2014).
282. L. A. Riedman, P. M. Sadler, Global species richness record and biostratigraphic potential of early to middle Neoproterozoic eukaryote fossils. *Precambrian Research* (2017).
283. P. A. Cohen, F. A. Macdonald, The Proterozoic record of eukaryotes. *Paleobiology* **41**, 610-632 (2015).
284. A. H. Knoll, E. J. Javaux, D. Hewitt, P. Cohen, Eukaryotic organisms in Proterozoic oceans. *Philosophical Transactions of the Royal Society of London B: Biological Sciences* **361**, 1023-1038 (2006).
285. G. Vidal, A. H. Knoll, Radiations and extinctions of plankton in the late Proterozoic and early Cambrian. *Nature* **297**, 57-60 (1982).
286. G. Vidal, M. Moczydłowska-Vidal, Biodiversity, speciation, and extinction trends of Proterozoic and Cambrian phytoplankton. *Paleobiology* **23**, 230-246 (1997).

287. R. M. Nagy, S. M. Porter, C. M. Dehler, Y. Shen, Biotic turnover driven by eutrophication before the Sturtian low-latitude glaciation. *Nature Geoscience* **2**, 415 (2009).
288. F. A. Corsetti, A. N. Olcott, C. Bakermans, The biotic response to Neoproterozoic snowball Earth. *Palaeogeography, Palaeoclimatology, Palaeoecology* **232**, 114-130 (2006).
289. K. Grey, M. R. Walter, C. R. Calver, Neoproterozoic biotic diversification: Snowball Earth or aftermath of the Acraman impact? *Geology* **31**, 459-462 (2003).
290. G. Williams *et al.*, The suppression of Antarctic bottom water formation by melting ice shelves in Prydz Bay. *Nature communications* **7**, 12577 (2016).
291. A. H. Orsi, S. S. Jacobs, A. L. Gordon, M. Visbeck, Cooling and ventilating the abyssal ocean. *Geophysical Research Letters* **28**, 2923-2926 (2001).
292. C. Murray, J. Riley (1969) The solubility of gases in distilled water and sea water—II. Oxygen. in *Deep Sea Research and Oceanographic Abstracts* (Elsevier), pp 311-320.
293. R. Weiss (1970) The solubility of nitrogen, oxygen and argon in water and seawater. in *Deep Sea Research and Oceanographic Abstracts* (Elsevier), pp 721-735.
294. A. Jenkins *et al.*, Observations beneath Pine Island Glacier in West Antarctica and implications for its retreat. *Nature Geoscience* **3**, 468 (2010).
295. P. D. Glynn, C. I. Voss, A. M. Provost, "Deep penetration of oxygenated meltwaters from warm based ice sheets into the Fennoscandian shield" in Use of hydrogeochemical information in testing groundwater flow models. (1999).
296. W. W. Fischer, J. Hemp, J. E. Johnson, Evolution of oxygenic photosynthesis. *Annual Review of Earth and Planetary Sciences* **44**, 647-683 (2016).
297. H. D. Holland, Volcanic gases, black smokers, and the Great Oxidation Event. *Geochimica et Cosmochimica Acta* **66**, 3811-3826 (2002).
298. N. J. Planavsky *et al.*, Evidence for oxygenic photosynthesis half a billion years before the Great Oxidation Event. *Nature Geoscience* **7**, 283 (2014).
299. T. A. Laakso, D. Schrag, A theory of atmospheric oxygen. *Geobiology* **15**, 366-384 (2017).
300. Y. Sekine *et al.*, Osmium evidence for synchronicity between a rise in atmospheric oxygen and Palaeoproterozoic deglaciation. *Nature communications* **2**, 502 (2011).
301. S. K. Sahoo *et al.*, Ocean oxygenation in the wake of the Marinoan glaciation. *Nature* **489**, 546 (2012).
302. G. M. Young, Precambrian supercontinents, glaciations, atmospheric oxygenation, metazoan evolution and an impact that may have changed the second half of Earth history. *Geoscience Frontiers* **4**, 247-261 (2013).
303. W. B. Berry, P. Wilde, Progressive ventilation of the oceans; an explanation for the distribution of the lower Paleozoic black shales. *American Journal of Science* **278**, 257-275 (1978).
304. P. A. P. Von Strandmann *et al.*, Selenium isotope evidence for progressive oxidation of the Neoproterozoic biosphere. *Nature communications* **6**, 10157 (2015).
305. K. V. Lau, F. A. Macdonald, K. Maher, J. L. Payne, Uranium isotope evidence for temporary ocean oxygenation in the aftermath of the Sturtian Snowball Earth. *Earth and Planetary Science Letters* **458**, 282-292 (2017).
306. A. Rodler *et al.*, Multiproxy isotope constraints on ocean compositional changes across the late Neoproterozoic Ghaub glaciation, Otavi Group, Namibia. *Precambrian Research* **298**, 306-324 (2017).
307. D. Fike, J. Grotzinger, L. Pratt, R. Summons, Oxidation of the Ediacaran ocean. *Nature* **444**, 744-747 (2006).
308. D. E. Canfield, S. W. Poulton, G. M. Narbonne, Late-Neoproterozoic deep-ocean oxygenation and the rise of animal life. *Science* **315**, 92-95 (2007).
309. H. Song *et al.*, The onset of widespread marine red beds and the evolution of ferruginous oceans. *Nature communications* **8**, 399 (2017).
310. J. B. Mertie, *The Tatonduk-Nation District, Alaska* (US Government Printing Office, 1932).

311. G. M. Yeo, The Rapitan Group: relevance to the global association of Late Proterozoic glaciation and iron-formation. (1984).
312. G. M. Young, Geochemical investigation of a Neoproterozoic glacial unit: the Mineral Fork Formation in the Wasatch Range, Utah. *Geological Society of America Bulletin* **114**, 387-399 (2002).
313. J. Keele, Upper Stewart River region, Yukon. *Geological Survey of Canada Annual Report* **1904**, 5-23 (1906).
314. J. Tang, H. Fu, Z. Yu, Stratigraphy, type and formation conditions of the Late Precambrian banded iron ores in South China. *Chinese Journal of Geochemistry* **6**, 331-341 (1987).
315. R. L. Jack, The iron ore resources of South Australia. *Geological Survey of South Australia, Bulletin* **9**, 71 (1922).
316. F. A. Macdonald, J. V. Strauss, C. V. Rose, F. Ő. Dudás, D. P. Schrag, Stratigraphy of the Port Nolloth Group of Namibia and South Africa and implications for the age of Neoproterozoic iron formations. *American Journal of Science* **310**, 862-888 (2010).
317. H. Martin, *The Precambrian geology of South West Africa and Namaqualand* (Precambrian Research Unit, University of Cape Town, 1965).
318. M. J. Kennedy, B. Runnegar, A. R. Prave, K.-H. Hoffmann, M. A. Arthur, Two or four Neoproterozoic glaciations? *Geology* **26**, 1059-1063 (1998).
319. A. Ilyin, Neoproterozoic banded iron formations. *Lithology and Mineral Resources* **44**, 78-86 (2009).
320. N. Chumakov, A problem of total glaciations on the Earth in the Late Precambrian. *Stratigraphy and Geological Correlation* **16**, 107 (2008).
321. B. Dzholdoshev, Stratigraphy of the Dzhetym-Too Formation within the Dzhetymskoe Iron Deposit, Tien Shan. *Issues of Precambrian and Lower Paleozoic Stratigraphy of Kirghizia*, 23-33 (1964).
322. M. Kianian, A. Khakzad (2008) Geochemistry of glaciogenic Neoproterozoic banded iron-formations from Kerman District (Iran). in *33rd International Geological Congress, Oslo, Abstracts, Session CGC-04*.
323. P. K. Sims, H. James, Banded iron-formations of late Proterozoic age in the central Eastern Desert, Egypt; geology and tectonic setting. *Economic Geology* **79**, 1777-1784 (1984).
324. E. Pelleter *et al.* (2006) Discovery of Neoproterozoic banded iron formation (BIF) in Morocco. in *European Geosciences Union General Assembly*.
325. N. Simpara, Etude géologique et structurale des unités externes de la chaine panafricaine (600 MA) des Dahomeyides dans la région de Bassar (Togo)', Travaux des Laboratoires des Sciences de la Terre, Série B, 13. *Marseilles: St Jérôme* (1978).
326. C. Gaucher, Sedimentology, palaeontology, and stratigraphy of the Arroyo del Soldado group..(Vendian to Cambrian, Uruguay). *Beringeria* (2000).
327. J. V. N. Dorr, Iron-formation in South America. *Economic Geology* **68**, 1005-1022 (1973).
328. G. d. Paiva, Código de Taxonomia—Ministério da Agricultura. *Divisão de Geologia e Mineralogia, Notas Preliminares e Estudos* (1940).
329. R. Trompette, C. De Alvarenga, D. Walde, Geological evolution of the Neoproterozoic Corumbágraben system (Brazil). Depositional context of the stratified Fe and Mn ores of the Jacadigo Group. *Journal of South American Earth Sciences* **11**, 587-597 (1998).
330. R. Trompette, Late Precambrian tillites of the Volta Basin and the Dahomeyides orogenic belt (Benin, Ghana, Niger, Togo and Upper-Volta). *Earth's Pre-Pleistocene Glacial Record*, 135-139 (1981).
331. E. Pecoits, M. Gingras, N. Aubet, K. Konhauser, Ediacaran in Uruguay: palaeoclimatic and palaeobiological implications. *Sedimentology* **55**, 689-719 (2008).
332. H. Atapour, A. Aftabi, The possible synglaciogenic Ediacaran hematitic banded iron salt formation (BISF) at Hormuz Island, southern Iran: Implications for a new style of exhalative hydrothermal iron-salt system. *Ore Geology Reviews* **89**, 70-95 (2017).

333. G. A. Gross, *Geology of iron deposits in Canada* (Department of Mines and Technical Surveys, Canada, 1965).
334. U. Upitis (1966) The Rapitan Group, Southeastern MacKenzie Mountains, Northwest Territories. (McGill University Libraries).
335. H. Gabrielse, Younger Precambrian of the Canadian Cordillera. *American Journal of Science* **272**, 521-536 (1972).
336. G. Eisbacher, Late Proterozoic rifting, glacial sedimentation, and sedimentary cycles in the light of Windermere deposition, western Canada. *Palaeogeography, Palaeoclimatology, Palaeoecology* **51**, 231-254 (1985).
337. J. H. Breitkopf, Iron formations related to mafic volcanism and ensialic rifting in the southern margin zone of the Damara Orogen, Namibia. *Precambrian research* **38**, 111-130 (1988).
338. H. Martin, Beobachtungen zum Problem der jung-praekambrischen glazialen Ablagerungen in Suedwestafrika. *Geologische Rundschau* **54**, 115-127 (1965).
339. L. Hurrey, Iron formations and glaciogenic sediments, Cornish Well, Olary, SA (BSc Hons Thesis). *School of Earth Sciences, The University of Melbourne* (1994).
340. G. M. Young, Iron-formation and glaciogenic rocks of the Rapitan Group, Northwest Territories, Canada. *Precambrian Research* **3**, 137-158 (1976).
341. D. E. Canfield, R. Raiswell, The evolution of the sulfur cycle. *American Journal of Science* **299**, 697-723 (1999).
342. N. L. Swanson-Hysell *et al.*, Cryogenian glaciation and the onset of carbon-isotope decoupling. *Science* **328**, 608-611 (2010).
343. L. R. Kump, W. E. Seyfried, Hydrothermal Fe fluxes during the Precambrian: effect of low oceanic sulfate concentrations and low hydrostatic pressure on the composition of black smokers. *Earth and Planetary Science Letters* **235**, 654-662 (2005).
344. Y. Goddéris *et al.*, The Sturtian 'snowball'glaciation: fire and ice. *Earth and Planetary Science Letters* **211**, 1-12 (2003).
345. G. M. Cox *et al.*, Continental flood basalt weathering as a trigger for Neoproterozoic Snowball Earth. *Earth and Planetary Science Letters* **446**, 89-99 (2016).
346. G. Yeo, Iron-formation, glaciation and global rifting in the Late Proterozoic. *Geol. Assoc. Can., Program with Abstracts* **8**, A76 (1983).
347. G. J. Baldwin, E. C. Turner, B. S. Kamber, M. Colpron, A new depositional model for glaciogenic Neoproterozoic iron formation: insights from the chemostratigraphy and basin configuration of the Rapitan iron formation. *Canadian Journal of Earth Sciences* **49**, 455-476 (2012).
348. A. J. Kaufman, J. Hayes, A. H. Knoll, G. J. Germs, Isotopic compositions of carbonates and organic carbon from upper Proterozoic successions in Namibia: stratigraphic variation and the effects of diagenesis and metamorphism. *Precambrian Research* **49**, 301-327 (1991).
349. G. M. Cox *et al.*, A model for Cryogenian iron formation. *Earth and Planetary Science Letters* **433**, 280-292 (2016).
350. M.-C. Liang, H. Hartman, R. E. Kopp, J. L. Kirschvink, Y. L. Yung, Production of hydrogen peroxide in the atmosphere of a Snowball Earth and the origin of oxygenic photosynthesis. *Proceedings of the National Academy of Sciences* **103**, 18896-18899 (2006).
351. J. L. Kirschvink, R. E. Kopp, Palaeoproterozoic ice houses and the evolution of oxygen-mediating enzymes: the case for a late origin of photosystem II. *Philosophical Transactions of the Royal Society B: Biological Sciences* **363**, 2755-2765 (2008).
352. G. M. Young, Proterozoic plate tectonics, glaciation and iron-formations. *Sedimentary Geology* **58**, 127-144 (1988).
353. K. L. Neale, Stratigraphy and geochemistry of Neoproterozoic iron formation, South Australia (PhD Thesis). *The University of Western Ontario* (1993).

354. P. F. Hoffman, 28th DeBeers Alex. Du Toit Memorial Lecture, 2004. On Cryogenian (Neoproterozoic) ice-sheet dynamics and the limitations of the glacial sedimentary record. *South African Journal of Geology* **108**, 557-577 (2005).
355. T. Gernon, T. Hincks, T. Tyrrell, E. Rohling, M. Palmer, Snowball Earth ocean chemistry driven by extensive ridge volcanism during Rodinia breakup. *Nature Geoscience* **9**, 242 (2016).
356. J. Calzia *et al.* (2000) Geologic map of the Kingston Range, southern Death Valley, California. (US Geological Survey).
357. B. L. Beard, C. M. Johnson, K. L. Von Damm, R. L. Poulson, Iron isotope constraints on Fe cycling and mass balance in oxygenated Earth oceans. *Geology* **31**, 629-632 (2003).
358. A. Bekker *et al.*, Iron formation: the sedimentary product of a complex interplay among mantle, tectonic, oceanic, and biospheric processes. *Economic Geology* **105**, 467-508 (2010).
359. V. McCoy, D. Asael, N. Planavsky, Benthic iron cycling in a high-oxygen environment: Implications for interpreting the Archean sedimentary iron isotope record. *Geobiology* **15**, 619-627 (2017).
360. J. Sun, X. Zhu, Z. Li, Confirmation and global significance of a large-scale early Neoproterozoic banded iron formation on Hainan Island, China. *Precambrian Research* **307**, 82-92 (2018).
361. A. Smith *et al.*, Oncoidal granular iron formation in the Mesoarchaean Pongola Supergroup, southern Africa: Textural and geochemical evidence for biological activity during iron deposition. *Geobiology* **15**, 731-749 (2017).
362. Z.-J. Zhou, H.-S. Tang, Y.-J. Chen, Z.-L. Chen, Trace elements of magnetite and iron isotopes of the Zankan iron deposit, westernmost Kunlun, China: A case study of seafloor hydrothermal iron deposits. *Ore Geology Reviews* **80**, 1191-1205 (2017).
363. N. Teixeira *et al.*, Trace elements and isotope geochemistry (C, O, Fe, Cr) of the Cauê iron formation, Quadrilátero Ferrífero, Brazil: Evidence for widespread microbial dissimilatory iron reduction at the Archean/Paleoproterozoic transition. *Precambrian Research* **298**, 39-55 (2017).
364. M. Mendes, L. M. Lobato, M. Kunzmann, G. P. Halverson, C. A. Rosière, Iron isotope and REE+ Y composition of the Cauê banded iron formation and related iron ores of the Quadrilátero Ferrífero, Brazil. *Mineralium Deposita* **52**, 159-180 (2017).
365. M. L. Lantink, P. B. Oonk, G. H. Floor, H. Tsikos, P. R. Mason, Fe isotopes of a 2.4 Ga hematite-rich IF constrain marine redox conditions around the GOE. *Precambrian Research* **305**, 218-235 (2018).
366. A. M. Satkoski, N. J. Beukes, W. Li, B. L. Beard, C. M. Johnson, A redox-stratified ocean 3.2 billion years ago. *Earth and Planetary Science Letters* **430**, 43-53 (2015).